



Toward RNA Life on Early Earth: From Atmospheric HCN to Biomolecule Production in Warm Little Ponds

Ben K. D. Pearce^{1,6} , Karan Molaverdikhani^{2,3,4,5} , Ralph E. Pudritz¹ , Thomas Henning³ , and Kaitlin E. Cerrillo¹

¹Origins Institute and Department of Physics and Astronomy, McMaster University, ABB 241, 1280 Main St, Hamilton, ON, L8S 4M1, Canada; bpearce6@jhu.edu

²Landessternwarte, Zentrum für Astronomie der Universität Heidelberg, Königstuhl 12, D-69117 Heidelberg, Germany

³Planet and Star Formation Department, Max Planck Institute for Astronomy, D-69117 Heidelberg, Germany

⁴Universitäts-Sternwarte, Ludwig-Maximilians-Universität München, Scheinerstrasse 1, D-81679 München, Germany

⁵Exzellenzcluster Origins, Boltzmannstraße 2, D-85748 Garching, Germany

Received 2021 November 23; revised 2021 December 25; accepted 2021 December 31; published 2022 June 8

Abstract

The origin of life on Earth involves the early appearance of an information-containing molecule such as RNA. The basic building blocks of RNA could have been delivered by carbon-rich meteorites or produced in situ by processes beginning with the synthesis of hydrogen cyanide (HCN) in the early Earth's atmosphere. Here, we construct a robust physical and nonequilibrium chemical model of the early Earth's atmosphere. The atmosphere is supplied with hydrogen from impact degassing of meteorites, water evaporated from the oceans, carbon dioxide from volcanoes, and methane from undersea hydrothermal vents, and in it lightning and external UV-driven chemistry produce HCN. This allows us to calculate the rain-out of HCN into warm little ponds (WLPs). We then use a comprehensive numerical model of sources and sinks to compute the resulting abundances of nucleobases, ribose, and nucleotide precursors such as 2-aminooxazole resulting from aqueous and UV-driven chemistry within them. We find that 4.4 billion years ago the limit of adenine concentrations in ponds for habitable surfaces is $0.05\ \mu\text{M}$ in the absence of seepage. Meteorite delivery of adenine to WLPs can provide boosts in concentration by 2–3 orders of magnitude, but these boosts deplete within months by UV photodissociation, seepage, and hydrolysis. The early evolution of the atmosphere is dominated by the decrease in hydrogen due to falling impact rates and atmospheric escape, and the rise of oxygenated species such as OH from H_2O photolysis. The source of HCN is predominantly from UV radiation rather than lightning. Our work points to an early origin of RNA on Earth within ~ 200 Myr of the Moon-forming impact.

Unified Astronomy Thesaurus concepts: Astrobiology (74); Pre-biotic astrochemistry (2079); Planetary atmospheres (1244); Earth (planet) (439); Lightning (2193)

1. Introduction

Astrophysical, geophysical, and fossil evidence suggests that life on Earth emerged in the interval of 4.5–3.7 bya (billion years ago) (Pearce et al. 2018). A fundamental question about the origin of life such as our own is whether biomolecular building blocks critical to creating information polymers such as RNA and proteins can be synthesized in situ on a habitable planet (Miller 1953). If not, then life's origin presumably depended on the delivery of biomolecules via external agents, such as carbon-rich meteorites (Chyba & Sagan 1992; Pearce et al. 2017; Damer & Deamer 2020).

HCN is a key biomolecule precursor because in aqueous solution it reacts with itself and other small molecules such as formaldehyde to produce several relevant biomolecules for the origin of RNA—widely thought to have been critical for the first life on Earth (Rich 1962; Gilbert 1986). One advantage of HCN over other more complex biomolecule precursors is that there are multiple favorable reaction pathways for its production directly from the dissociation products of common atmospheric gases, i.e., N_2 , CH_4 , and H_2 (Pearce et al.

2020b). The famous Miller–Urey experiments showed that reducing atmospheres rich in H_2 and CH_4 are favorable for HCN production, whereas oxidizing atmospheres rich in CO_2 do not produce as much HCN (Miller 1957a; Schlesinger & Miller 1983; Benner et al. 2020). This is because oxygen must be removed from oxidized carbon (i.e., CO_2 and CO) before it can react to form HCN, which is energetically expensive. Reduced carbon (e.g., CH_4 , CH_3), on the other hand, directly reacts to produce HCN (Pearce et al. 2020a, 2020b; Catling & Kasting 2007). It is the HCN produced by electrical discharges, once dissolved in the water reservoir in the Miller–Urey apparatus, that produces the plethora of amino acids (Miller 1957b; Bada 2013) and nucleobases (Ferus et al. 2017b; Becker et al. 2018).

However, such experiments do not address the whole planetary and geochemical context of an evolving planet and its atmosphere, nor do they address what conditions actually lead to RNA synthesis sufficient for an RNA world. Given the multiple processes that contribute to the balance of H_2 , CH_4 , and CO_2 in the early Earth atmosphere, including volcanic outgassing, asteroid impacts, hydrothermal activity in undersea vents, hydrogen escape from the atmosphere, and rain-out, what are the yields of biomolecules in specific environments?

Several invaluable observations are available to constrain early Earth conditions. The analysis of a zircon mineral inclusion has shown that the early mantle was already oxidized by ~ 4.35 bya. This implies that by then, volcanoes mainly outgassed CO_2 (Trail et al. 2011). Before 4.35 bya, isotopic

⁶ Current address: Department of Earth and Planetary Science, Johns Hopkins University, Baltimore, MD 21218, USA.



evidence from the Earth’s mantle (nitrogen, oxygen, titanium, calcium, chromium, nickel, ruthenium, molybdenum, neodymium, and deuterium) shows that accreting material was most similar to enstatite meteorites (Dauphas 2017; Piani et al. 2020). Reduced iron from these impactors would have been oxidized by water, releasing H_2 (Zahnle et al. 2020). We note that recent isotopic studies suggest that substantial amounts of carbonaceous-chondrite-like materials were present in these impactors as well (Zahnle et al. 2020). Past models predict that the early Earth atmosphere had a slightly reducing composition dominated by species such as N_2 , CO_2 , CH_4 , CO , and H_2 (Zahnle 1986; Tian et al. 2011; Zahnle et al. 2020).

The ultimate step—actual RNA synthesis—could occur naturally in warm little ponds (WLPs) on the small land area available on the planet at that time (McCulloch & Bennett 1993). The crucial point is that in the absence of any biological enzymes, bond formation that leads to RNA polymers involves thermal energy sufficient to remove water between the nucleotide building blocks. Such condensation reactions are well studied experimentally and arise naturally during seasonal or daily wet–dry cycles in WLPs (Morasch et al. 2014; Da Silva et al. 2015; Ross & Deamer 2016; Pearce et al. 2017; Yi et al. 2020).

The route to nucleotides remains a big question in prebiotic chemistry. The older approach involved reacting nucleobases, ribose, and a phosphorus source, which leads to low yields (Ponnamperuma et al. 1963). A more recent and radically different method bypasses the need for nucleobases and ribose reactants to obtain nucleotides, requiring simpler reactants of unknown concentration on early Earth such as glycolaldehyde, cyanamide, glyceraldehyde, and cyanoacetylene (Powner et al. 2009). The key intermediate in the latter pathway, sometimes referred to as the Powner–Sutherland approach, is 2-aminooxazole. 2-aminooxazole can also be formed by irradiating solutions of HCN to produce formaldehyde, which then reacts with another HCN molecule to produce glycolonitrile. Glycolonitrile then reacts further in the presence of aqueous HCN to produce glycolaldehyde and glyceraldehyde, two of the starting components of the Powner–Sutherland approach. Irradiating aqueous HCN in the presence of molar concentrations of NaCl and NH_4Cl salts produces cyanamide, another key reactant for this approach (Yi et al. 2020).

Another recent approach to nucleotide formation involves wet–dry cycling of malononitrile and amidinium salts, the former of which could come from HCN-based reactions in WLPs (Becker et al. 2018). Finally, a route to the DNA nucleotides has been discovered by reacting nucleobases with acetaldehyde and the subsequent reaction with formaldehyde or glycolaldehyde (Teichert et al. 2019). Due to the uncertainty in the main prebiotic route to nucleotides, we take an agnostic approach and compute the WLP concentrations of nucleobases, ribose, and 2-aminooxazole produced via HCN aqueous chemistry driven by ultraviolet (UV) irradiation.

The ultimate source of HCN is from nonequilibrium photochemical and lightning-based reactions in the early Earth atmosphere. It has been modeled for a range of initial concentrations of key primordial species such as CH_4 and CO_2 (Zahnle 1986; Tian et al. 2011). Furthermore, experiments involving electric discharges in reducing early Earth conditions have produced high abundances of HCN (Ferus et al. 2017a). Most recently, rare, very large impactors (~ 400 km) have been proposed as a source of enormous yields of HCN (Genda

et al. 2017; Benner et al. 2020; Zahnle et al. 2020). These early large impacts generate both the reducing conditions and the sustained high temperatures required to produce substantial CH_4 , the main precursor to HCN. Very large impactors are also one logical explanation for the discrepancy between the highly siderophile element (HSE) signatures in the lunar and terrestrial mantles (Genda et al. 2017). However, impactors of such a large size are not necessarily a good solution for the origin of life. The energy from these impactors produces sustained high surface temperatures and pressures that render the planet uninhabitable (see Section 4). This would be a world devoid of ponds. Furthermore, the largest lunar impactor was ~ 200 km in size—as seen in the cratering record—so it is expected that few objects greater than 300 km would have impacted early Earth (Sleep 2010).

Here, we develop a holistic nonequilibrium atmosphere–pond coupled chemistry model that offers multiple important advancements to these past models. Instead of considering atmospheric processes individually, we build a comprehensive model that includes lightning, photochemistry, impact degassing, volcanism, ocean geochemistry, and ocean evaporation simultaneously. We employ a newly extended disequilibrium atmospheric chemistry code that is augmented with new, expanded HCN and formaldehyde chemistry to follow atmospheric chemical evolution. These simulations are also informed by computed self-consistent pressure–temperature (P – T) profiles via radiative transfer. The resulting computed HCN rain-out to surface WLPs drives the subsequent aqueous reactions of HCN into various critical biomolecules in the face of key terrestrial sinks such as hydrolysis, seepage, and UV photodestruction. The origin of formaldehyde (H_2CO) is also important to pin down as it is necessary for the formation of ribose, the pyrimidine nucleobases, and 2-aminooxazole.

2. Methods

2.1. Early Earth Atmospheric Model

In Figure 1, we illustrate our early Earth atmospheric models by focusing on the main sources and sinks for the key molecular species relevant to controlling and determining HCN chemistry. As an overall principle, H_2 and CO_2 are the main species that determine whether the environment is reducing or oxidizing. It is the balance between these two species that determines the concentration of CH_4 , the main precursor to HCN.

In the top left panel, impact degassing produces H_2 . The degassing rate at each epoch is calculated by combining equilibrium H_2 production rates from enstatite chondrite impactors via the reaction $\text{Fe} + \text{H}_2\text{O} \rightarrow \text{FeO} + \text{H}_2$ (Zahnle et al. 2020) with the bombardment rate on early Earth based on mathematical fits to the observed lunar cratering record (Chyba 1990; Pearce et al. 2017). The main sinks for H_2 include UV photodissociation, hydrodynamic escape to space, and disequilibrium chemistry.

In the top right panel, the main source of CO_2 on early Earth is volcanic outgassing (Zahnle et al. 2020). We use a constant Earth-like volcanic CO_2 outgassing rate in all our models (Hu et al. 2012). The main sinks for CO_2 are photodissociation in the upper atmosphere and rain-out in the lower atmosphere.

We utilize a potentially abundant source of CH_4 to the Hadean atmosphere from serpentization and Fischer–Tropsch-type (FTT) synthesis. This begins with water-

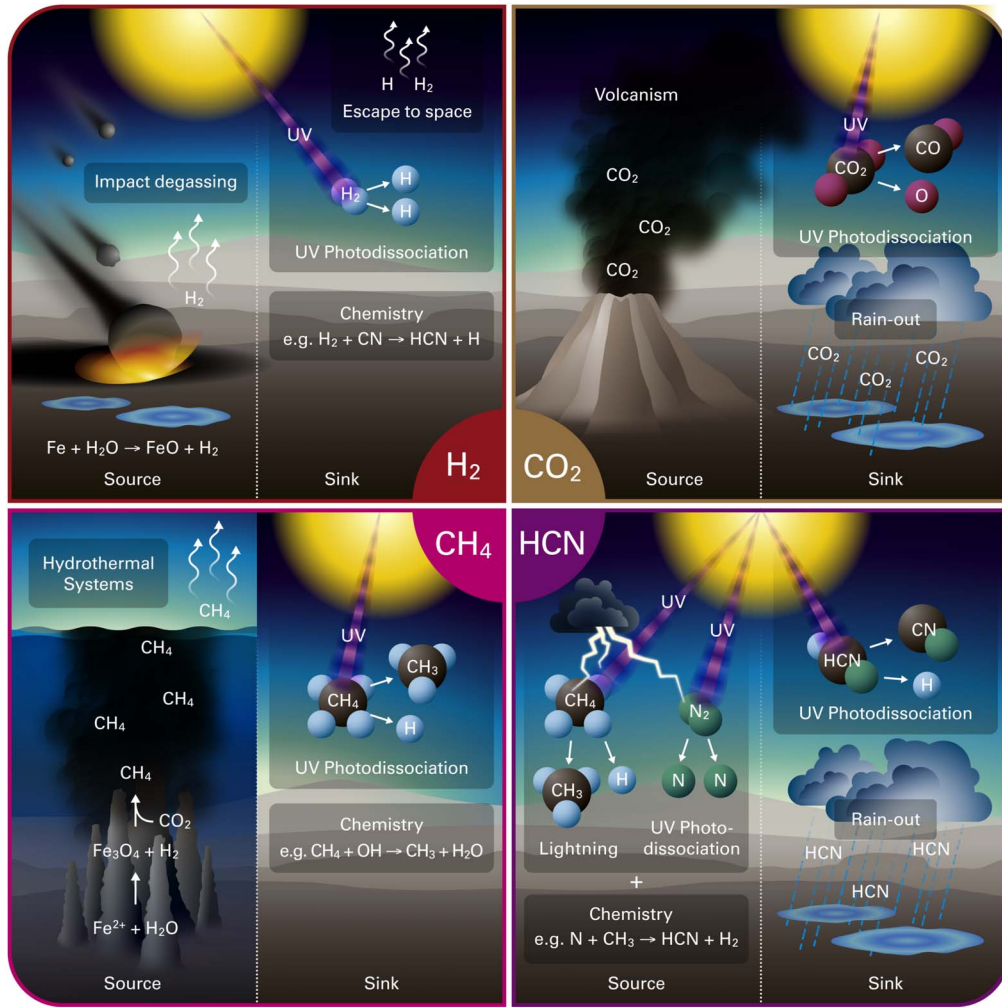


Figure 1. An illustration of the sources and sinks of the four key species in our atmospheric model: H_2 , CO_2 , CH_4 , and HCN .

dependent processes in hydrothermal systems wherein Fe- and Mg-rich ultramafic rocks (e.g., olivine) in mid-ocean ridges and forearc systems produce H_2 . Then, H_2 reacts with the aqueous CO_2 in these environments in the presence of mineral catalysts to produce CH_4 (Holm et al. 2015; Guzmán-Marmolejo et al. 2013). Abiotic methane production has been observed in hydrothermal systems (Fiebig et al. 2007; Bradley & Summons 2010); however, experiments of FTT synthesis from olivine typically produce very low yields (Krissansen-Totton et al. 2018). Naturally occurring catalysts such as awaruite or chromite greatly speed up FTT synthesis (Bradley 2016); however, the availability of these catalysts in primordial hydrothermal systems is still somewhat uncertain. Equilibrium models suggest this hydrothermal process can sustain $\sim 2\text{--}2.5$ parts per million (ppm) of CH_4 in the early atmosphere (Guzmán-Marmolejo et al. 2013). We use the calculated CH_4 outgassing rate from these models (Guzmán-Marmolejo et al. 2013). The main sinks for methane are UV photodissociation and disequilibrium chemistry.

Finally, the main source of HCN is photodissociation or lightning dissociation of species such as N_2 and CH_4 followed by radical chemistry. In the case of lightning, this radical chemistry takes place at high temperature in the lightning channel. The main sinks for HCN are UV photodissociation

and rain-out. For further details on the source and sink rates, see Appendix A.

We model the early Earth atmosphere during its reducing phase at 4.4 bya for calculated habitable surface temperatures of 78°C (Model A) and 51°C (Model C), as well as its oxidizing phase at 4.0 bya for calculated surface temperatures of 51°C (Model B) and 27°C (Model D). These particular surface temperatures result from the radiative transfer calculations for our chosen starting atmospheric compositions. These models differ in atmospheric composition, solar luminosity, UV irradiation intensity, HCN and radical production from lightning, and impact bombardment rate (see Table 1 for model details).

2.2. Nonequilibrium Atmospheric Chemistry

ChemKM is a spatially 1D chemical kinetic model for disequilibrium atmospheric chemistry calculations that makes use of the Double-precision Livermore Solver for Ordinary Differential Equations (DLSODE) from the ODEPACK collection (Stpleman 1983). The error for this solver is controlled by the relative error tolerance and the absolute error tolerance, which are set to 10^{-5} and 10^{-99} respectively to ensure numerical stability.

Table 1
Summary of the Four Early Earth Atmospheric Models in This Work

Model	Description	Date (bya)	P_s (bar) ^a	T_s (°C) ^b	Molar Composition	Surface Flux (cm ⁻² s ⁻¹)	Lightning (cm ⁻² s ⁻¹) ^c
A	Early Hadean (reducing)	4.4	1.5	78	H ₂ : 90% N ₂ : 10% CH ₄ : 2 ppm H ₂ O: Figure A1	H ₂ : 2.3×10^{11} CO ₂ : 3.0×10^{11} CH ₄ : 6.8×10^8 H ₂ O: 2.0×10^9	H: 4.1×10^6 CO: 6.3×10^3 OH: 4.4×10^3 NO: 5.0×10^1 ³ O: 4.4×10^0 ⁴ N: 7.2×10^{-1} HCN: 4.4×10^{-1} O ₂ : 2.2×10^{-2} CH ₃ : 1.6×10^{-3}
B	Late Hadean (oxidizing)	4.0	2	51	CO ₂ : 90% N ₂ : 10% CH ₄ : 10 ppm H ₂ O: Figure A1	H ₂ : 2.3×10^{10} CO ₂ : 3.0×10^{11} CH ₄ : 6.8×10^8 H ₂ O: 2.0×10^9	CO: 1.8×10^5 O ₂ : 8.5×10^4 NO: 7.4×10^3 OH: 3.5×10^3 ³ O: 5.5×10^2 H: 9.7×10^1 ⁴ N: 3.2×10^{-3} HCN: 2.9×10^{-6}
C	Early Hadean (reducing)	4.4	1.13	51	H ₂ : 90% N ₂ : 10% CH ₄ : 1 ppm H ₂ O: Figure A1	H ₂ : 2.3×10^{11} CO ₂ : 3.0×10^{11} CH ₄ : 6.8×10^8 H ₂ O: 2.0×10^9	H: 1.1×10^5 OH: 1.3×10^2 CO: 8.1×10^1 NO: 1.6×10^0 ³ O: 1.6×10^{-1} ⁴ N: 2.2×10^{-2} HCN: 4.1×10^{-3} O ₂ : 7.4×10^{-4} CH ₃ : 1.3×10^{-5}
D	Late Hadean (oxidizing)	4.0	2	27	CO ₂ : 90% N ₂ : 10% CH ₄ : 1.5 ppm H ₂ O: Figure A1	H ₂ : 2.3×10^{10} CO ₂ : 3.0×10^{11} CH ₄ : 6.8×10^8 H ₂ O: 2.0×10^9	CO: 1.8×10^5 O ₂ : 8.5×10^4 NO: 7.4×10^3 OH: 3.5×10^3 ³ O: 5.5×10^2 H: 9.7×10^1 ⁴ N: 3.2×10^{-3} HCN: 2.9×10^{-6}

Notes. Initial compositions for each model are chosen to (a) align with typical assumptions for reducing (H₂-dominant) or oxidizing (CO₂-dominant) conditions at the chosen epoch, and (b) yield calculated P – T profiles with habitable surface conditions (i.e., $0^\circ\text{C} \leq T_s \leq 100^\circ\text{C}$) (see Figure A2 for P – T profiles).

^a P_s : surface pressure.

^b T_s : surface temperature.

^c ³O and ⁴N represent the triplet and quartet spin states for oxygen and nitrogen atoms, respectively. Our chemical network also includes singlet oxygen (¹O) and doublet nitrogen (²N).

ChemKM computes atmospheric chemistry based on input chemical network, P – T profile, eddy diffusion (mixing) profile, top-of-atmosphere (TOA) solar radiation, wavelength-dependent photochemical reactions, and influxes and outfluxes of species at the surface and TOA. ChemKM has been benchmarked with several other chemical kinetic codes,⁷ and has been used in the past to simulate the atmosphere of Titan (Pearce et al. 2020b), as well as those of cold, hot, and ultrahot gaseous exoplanets (Molaverdikhani et al. 2019a, 2020a). Atmospheric rain-out was newly developed in ChemKM for this work. Simulations were run on the cluster for approximately one week. In this time, our models reached 1–50 million years of simulated time.

CRAHCN-O is a consistent reduced atmospheric hybrid chemical network now containing 259 two- and three-body reactions for the production of HCN and H₂CO in atmospheres

dominated by any of H₂, CO₂, N₂, CH₄, and H₂O. We introduce 28 new reactions to CRAHCN-O in this work, in order to avoid the atmospheric buildup of species that previously had no reaction sinks (see Tables A1 and A2 for details). We have tested an oxygenless version of this network (CRAHCN) by modeling HCN production in Titan’s atmosphere, and our computed HCN profile agreed very well with the Cassini observations (Pearce et al. 2020b).

2.3. Atmospheric Pressure–Temperature Profiles

petitRADTRANS is a 1D radiative transfer code based on the correlated- k method for gas absorption and the Guillot temperature model (Guillot 2010; Mollière et al. 2019). It is typically used to model exoplanet atmospheres to obtain transmission and thermal spectra (e.g., Molaverdikhani et al. 2019a; Mollière et al. 2020; Wang et al. 2020). We build upon its existing functionality to calculate P – T profiles self-

⁷ <https://www.issibern.ch/teams/1dchemkinetics/>

consistently with tropospheric water vapor in sequence with the Arden Buck equation (Buck 1981).

P – T structure calculations are performed using petitRADTRANS (Mollière et al. 2019), and atmospheric chemistry is calculated using ChemKM (Molaverdikhani et al. 2019a, 2020a) coupled with an updated version of the CRAHCN-O chemical network (Pearce et al. 2020a, 2020b). We are the first to calculate composition-dependent P – T profiles for modeling HCN chemistry in the early Earth atmosphere. Past models have used a general habitable P – T profile or estimated the surface temperature using an analytic equation for a moist adiabat (Zahnle 1986; Tian et al. 2011; Zahnle et al. 2020). The code used to compute P – T profiles is available at <https://gitlab.com/mauricemolli/petitRADTRANS>.

For complete details on our atmospheric models, see Appendix A.

2.4. Lightning Production of Molecules

We follow the thermodynamic treatment from Chameides & Walker (1981) for the lightning production of HCN and other species on early Earth. Based on our initial atmospheric compositions, we calculate the equilibrium abundances of HCN, H_2 , N_2 , H_2O , CO_2 , CH_4 , O_2 , NO , OH , H , 4N , CO , 3O , and CH_3 , in a 1 cm^2 lightning channel extending through the lowest layer in our atmospheres at a freeze-out temperature $T_F = 2000\text{ K}$. We use thermochemical data from the JANAF tables (Stull & Prophet 1971), and the ChemApp Software library for Gibbs free energy minimization (distributed by GTT Technologies, <http://gtt.mch.rwth-aachen.de/gtt-web/>).

We then use the resultant mixing ratios to calculate the influx of each of these species into the lowest layer of our atmospheres. These species were chosen because they are dominant equilibrium products in the early Earth lightning models by Chameides & Walker (1981). The freeze-out temperature (T_F) was chosen to most accurately model the HCN produced in a lightning strike, as this is the key species of interest in this paper. Although freeze-out temperatures typically range from 1000–5000 K across species, one freeze-out temperature must be chosen to conserve the elemental abundances in the lightning strike. A nonequilibrium approach was also considered; however, an extensive high-temperature (up to 30,000 K) chemical kinetic network would be required and is perhaps unnecessary given the equilibrium timescale of $<1\text{ }\mu\text{s}$ above 10,000 K compared to the $\sim 10\text{ }\mu\text{s}$ timescale of eddy diffusion and the $\sim 100\text{ ms}$ cooling time of a lightning channel (Hill et al. 1980).

2.5. Complete Impact–Atmosphere–Ocean Coupling Models

The main assumption of our models is that the surface of the Earth maintained habitability (i.e., $0^\circ\text{C} < T < 100^\circ\text{C}$), which is key for the presence of WLPs and the origin of life. We begin with assumed reducing and oxidizing atmospheric compositions for the early and late Hadean, respectively, and calculate the initial P – T profiles and tropospheric water vapor based on these compositions. We adjust both initial methane concentration and surface pressure to obtain calculated temperature profiles that fall within the habitable range. We smooth the initial water profiles from our calculations to 1% at the surface, and include ocean–atmosphere coupling by imposing an ocean evaporation rate of $2 \times 10^9\text{ cm}^2\text{ s}^{-1}$ to maintain a water mixing ratio of $\sim 0.1\%$ – 1% at the surface.

In Table 1, we summarize the four early Earth atmospheric models in our study. We model two epochs that vary in atmospheric composition, solar luminosity, UV irradiation intensity, and asteroid bombardment rate. These models correspond to the early Hadean at 4.4 bya (billion years ago) and the late Hadean at 4.0 bya. We compute two habitable P – T profiles for each model by slightly adjusting the methane content and/or surface pressure. The luminosity, UV intensity, and asteroid bombardment rate at each epoch are based on stellar evolution models (Heller et al. 2020; Baraffe et al. 2015), observations of solar analogs (Ribas et al. 2005), and the lunar cratering record (Chyba 1990), respectively.

2.6. Biomolecule Chemistry in Warm Little Ponds: Sources and Sinks

Our atmospheric models are coupled (via rain-out) with the sources and sinks WLP model we first developed in Pearce et al. (2017). Biomolecule abundances are described by first-order linear differential equations and are solved numerically. The evolving concentrations of nucleobases, ribose, formaldehyde, and 2-aminooxazole in our WLP models are driven by the rate of incoming HCN from rain-out, and biomolecule losses due to UV dissociation, seepage, and hydrolysis. Given that experimental reaction rates are fast (\lesssim a few days), we apply experimental reaction yields to our HCN pond concentrations in order to estimate the pond concentrations of formaldehyde, nucleobases, ribose, and 2-aminooxazole. However, we recognize that at the lower pond concentrations here, these reactions could take much longer. The code used to compute biomolecule concentrations in ponds is available at https://github.com/bennski/Wet_Dry_Cycling_Pond_Model.

We utilize the experimental result that UV irradiation of liquid water produces solvated electrons, enabling a chemical pathway from HCN to formaldehyde (H_2CO) (Yi et al. 2020) in ponds. H_2CO can also enter ponds directly from the atmosphere (Pinto et al. 1980). Aqueous solutions containing HCN and H_2CO can produce nucleobases (i.e., adenine, guanine, cytosine, uracil, thymine) (Oró 1961; Larowe & Regnier 2008; Ferus et al. 2019), which are the base-pairing components of RNA and DNA, as well as ribose (Butlerow 1861; Breslow 1959), which binds with phosphate to make up the RNA backbone.

Furthermore, irradiated and wet–dry cycled or flowing solutions of HCN in the presence of phosphorus and dissolved salts enable the production of 2-aminooxazole, a key intermediate in the Powner–Sutherland pathway for producing the pyrimidine building blocks of RNA (cytidine and uridine monophosphate) (Powner et al. 2009; Ritson et al. 2018; Yi et al. 2020). Finally, Becker et al. (2018) recently presented a pathway to RNA nucleosides that involves the wet–dry cycling of solutions containing HCN and other atmospheric precursors. Such prebiotic chemistry experiments and models are based on the assumption that species such as HCN and H_2CO would be present and concentrated in WLPs on early Earth.

We considered including formose-like reactions occurring from more complex aldehydes (e.g., glycolaldehyde, glyceraldehyde) (Cassone et al. 2018); however, given the greater complexity of these species, it is expected that they would be produced in the atmosphere in much lower concentrations than HCN and H_2CO . However, it would be valuable to explore reactions that produce these more complex aldehydes in

planetary atmospheres so that these sugar precursors can be included in a future model.

Lastly, we understand that straightforwardly applying experimental biomolecule production yields from HCN to obtain estimates of biomolecule influxes in our WLP model has issues given the high reactant concentrations and ideal conditions of each experimental setup; however, given that there are no chemical kinetic rate coefficients for the aqueous production of nucleobases, ribose, and 2-aminooxazole, we utilize experimental yields in our model to obtain reasonable first-order estimates. We emphasize that these biomolecule concentrations should be understood as upper bounds in the absence of any concentrating mechanism beyond evaporation.

In Table A6 we summarize the sources and sinks of our pond models. See Appendix A.2 and Pearce et al. (2017) for complete details regarding these models.

2.7. Wet-Dry Cycling in WLPs

We have found that ponds that are roughly 1 m in radius and depth and are cylindrical in shape are an optimal fiducial estimate for subsequent RNA polymer synthesis by wet-dry cycles (Pearce et al. 2017). We use the “intermediate” hot early Earth environment from Pearce et al. (2017), which is based on the seasonal sinusoidal precipitation rates in Indonesia (Reichle et al. 2011; Berghuijs & Woods 2016). Precipitation coupled with evaporation and seepage produces a natural wet-dry cycle within the pond that has a ~ 6 month wet phase followed by a ~ 6 month dry phase. Various pond environments were explored in Pearce et al. (2017), and were found to produce similar results in terms of peak nucleobase concentrations.

3. Results

3.1. Atmospheric HCN and H_2CO

In Figures 2(A), (B), (C), and (D), we plot the temporal evolution of atmospheric HCN and H_2CO in these four early Earth models. To give some context for what would be considered high atmospheric HCN abundances, Cassini observed HCN mixing ratios in the heavily reducing atmosphere of Titan to be $\sim 10^{-7}$ – 10^{-6} near the surface (150–300 km) and $\sim 10^{-4}$ – 10^{-2} in the upper atmosphere (700–1050 km) (Magee et al. 2009; Vinatier et al. 2010; Adriani et al. 2011; Koskinen et al. 2011).

In the early Hadean (reducing) model A, HCN mixing ratios decrease from 10^{-11} at the surface to 10^{-14} from $t = 100$ yr to 400 yr. Then, HCN slowly builds back up again to 2.7×10^{-11} over the next 50 million years. Moving up in altitude, we see the main region of HCN production from UV radiation at ~ 500 – 600 km, which provides an HCN abundance of $\sim 10^{-7}$ – 10^{-6} at these altitudes after 10 million years. We isolate the predominant energy source for HCN production in Figures 2(E) and (F) by turning off UV photochemistry and lightning chemistry, respectively, for our early Hadean (reducing) model A.

In the late Hadean (oxidizing) model B, HCN mixing ratios decrease at the surface from 10^{-14} to 10^{-16} from $t = 100$ yr to $\sim 40,000$ yr. Then, HCN slowly builds back up to 10^{-15} over the next 2 million years. UV production of HCN produces a peak abundance of $\sim 10^{-8}$ at ~ 50 km at 2 million years.

One of the most important results is that neither oxidizing model produces nearly as much HCN as our reducing models. Our calculations reveal that HCN production near the surface is

about four orders of magnitude more favorable in reducing conditions than it is in oxidizing conditions. It is worth noting that the oxidizing conditions at 4.0 bya have reduced gases such as H_2 in the ppb–ppm range. Even more oxidizing conditions could be present after 4.0 bya with the declining H_2 impact degassing rate allowing oxygen species to become more dominant.

We learned that UV photochemistry is crucial for atmospheric HCN production on early Earth (Figures 2(E) and (F)). A major result of our simulations is that without UV photochemistry, HCN would be over eight orders of magnitude less abundant at the surface during the early Hadean. Even with an increased lightning flash density representative of storms occurring during volcanic eruptions (1×10^4 flashes km^{-2} yr^{-1} , Hodosán et al. 2016), we see no enhancement in HCN concentration beyond the photochemical result (see Figure B4).

Formaldehyde, given these atmospheric models, would need to come from elsewhere, such as UV-driven, aqueous chemistry in WLPs. In comparison to HCN, H_2CO is much less abundant at the surface in our early Hadean (reducing) models. H_2CO builds up from $\sim 10^{-23}$ to $\sim 10^{-16}$ over 50 million years. The mixing ratio for H_2CO is at its highest value of 10^{-9} – 10^{-8} in the middle of the atmosphere of these models after 50 million years. In the late Hadean (oxidizing) model B, H_2CO increases at the surface from $\sim 10^{-16}$ to $\sim 10^{-13}$ in ~ 1 million years. We did not explore atmospheric production of H_2CO further given its considerably low abundances in all models.

3.2. Surface Abundances

The temporal evolution of the dominant atmospheric species at the lowest (surface) layer in the atmosphere is shown in Figure 3. The atmospheric rain-out rates for HCN and H_2CO from this layer provides the influx rates into the WLPs.

One striking result of our atmospheric chemistry calculations is that the HCN and CH_4 mixing ratios are correlated after the first few hundred years in all our models. The relevant abundance curves are shown in bold in Figure 3 to emphasize this point, as the HCN and CH_4 abundances trace one another closely from $t = 300$ yr onward.

In Figure B2, we plot the molar ratio of HCN to CH_4 over time and find an average value of $\sim (1\text{--}4) \times 10^{-7}$ for the early Hadean (reducing) models and $(3\text{--}5) \times 10^{-6}$ for the late Hadean (oxidizing) models.

CH_4 and HCN surface abundances also follow the trend of the H_2 surface abundances in the late Hadean (oxidizing) models B and D. This is because H_2 drives the evolution of reducing and oxidizing conditions in our models. We see that CH_4 abundances are stable in reducing (high H_2) conditions, and that CH_4 abundances are depleted in oxidizing (high O_2 and OH) conditions.

There is an anticorrelation between HCN and O_2 in the late Hadean (oxidizing) models. This is because a high O_2 environment leads to the oxidation of carbon into species such as H_2CO rather than the reduction of carbon into HCN. This is also why we also see a correlation between O_2 and H_2CO in the late Hadean (oxidizing) models.

These correlations and anticorrelations are consistent with the atmospheric observations we see for Titan and present-day Earth, respectively. Titan’s atmosphere is abundant in HCN (10^{-7} – 10^{-2}) (Vinatier et al. 2010; Adriani et al. 2011; Koskinen et al. 2011; Magee et al. 2009) due to the high abundances of reducing gases such as CH_4 ($\sim 5.7\%$) and H_2

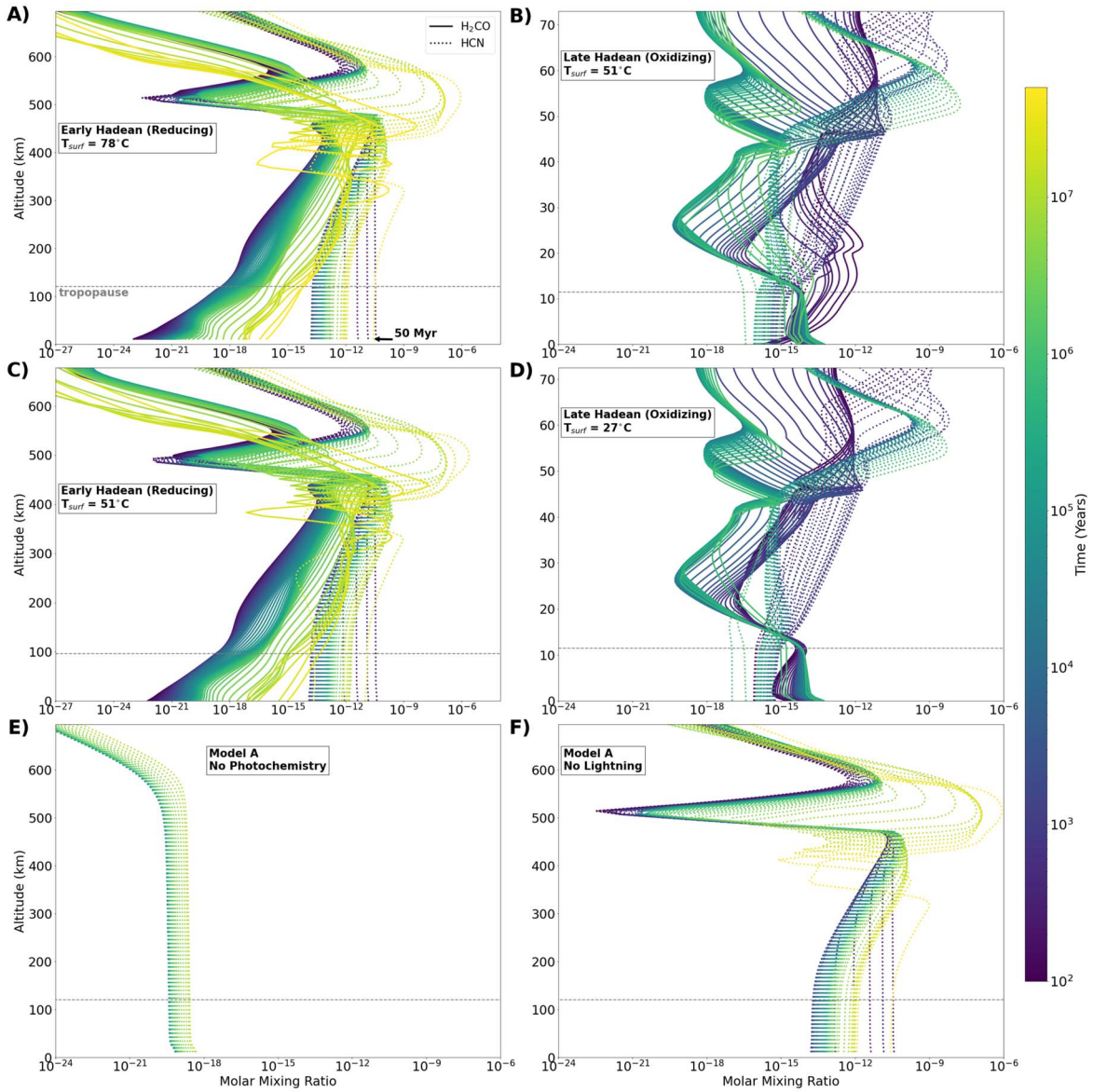


Figure 2. (A)–(D) H_2CO and HCN atmospheric mixing ratios from $t = 100$ yr to 1–50 million years for the four early Earth models listed in Table 1. Pressures go from 1.13–2 bar at the surface to 10^{-8} bar at the top of the atmosphere. Atmospheric scale heights vary primarily due to differences in mean molecular weight. The tropopause is labeled and corresponds to a pressure of ~ 0.14 bar. (E) HCN atmospheric mixing ratio from $t = 100$ yr to 13 million years for model A with photochemistry turned off. (F) HCN atmospheric mixing ratio from $t = 100$ yr to 50 million years for model A with lightning chemistry turned off.

($\sim 0.1\%$) and low concentrations of oxidizing gases such as CO_2 (10–20 ppb) and H_2O (0.5–8 ppb) (Catling 2015; Hörst 2017). On the other hand, HCN on Earth today is present in low abundances $\sim 10^{-10}$ (Cicerone & Zellner 1983) because of the high abundance of oxidizing gases in our atmosphere such as O_2 (21%), H_2O (0%–3%), and CO_2 (~ 400 ppm) and modest ~ 1 ppm levels of CH_4 .

We tested the hypothesis presented in several exo-atmosphere studies that the C/O ratio plays a central role in controlling their chemical composition (Madhusudhan 2012; Mollière et al. 2015; Rimmer & Rugheimer 2019; Molaverdikhani et al. 2019a, 2019b, 2020b). In our early Hadean (reducing) models, the C/O ratio in the lowest atmospheric layer increases from 10^{-3} to 10^{-2} in the first few thousand years, and then to 1 after ~ 30 million years. In the late Hadean (oxidizing) models, the C/O ratio decreases from 0.5 to $\sim 10^{-2}$ in the first few thousand years, and then increases to 0.02–0.03

over the next 1–2 million years. Evidently the C/O ratios in our models are set mainly by the increase and decrease of CO_2 and CO at the surface, and in the late Hadean (oxidizing) models, also by the fluctuation of O_2 . Our models show that the abundances of key biomolecule precursor species CH_4 and HCN are not strongly dependent on the C/O ratio.

These results are not entirely surprising. In a study of the effects of C/O ratio on atmospheric HCN abundance, Rimmer & Rugheimer (2019) found that for a given C/O ratio, the presence of methane leads to considerably more HCN . Considering these results, we suggest that CH_4 abundance is a better fundamental driver for HCN production than the C/O ratio on its own.

3.3. Biomolecule Concentrations in WLPs

In Figure 4(A), we display the concentrations of adenine in our model WLP from aqueous production for different HCN

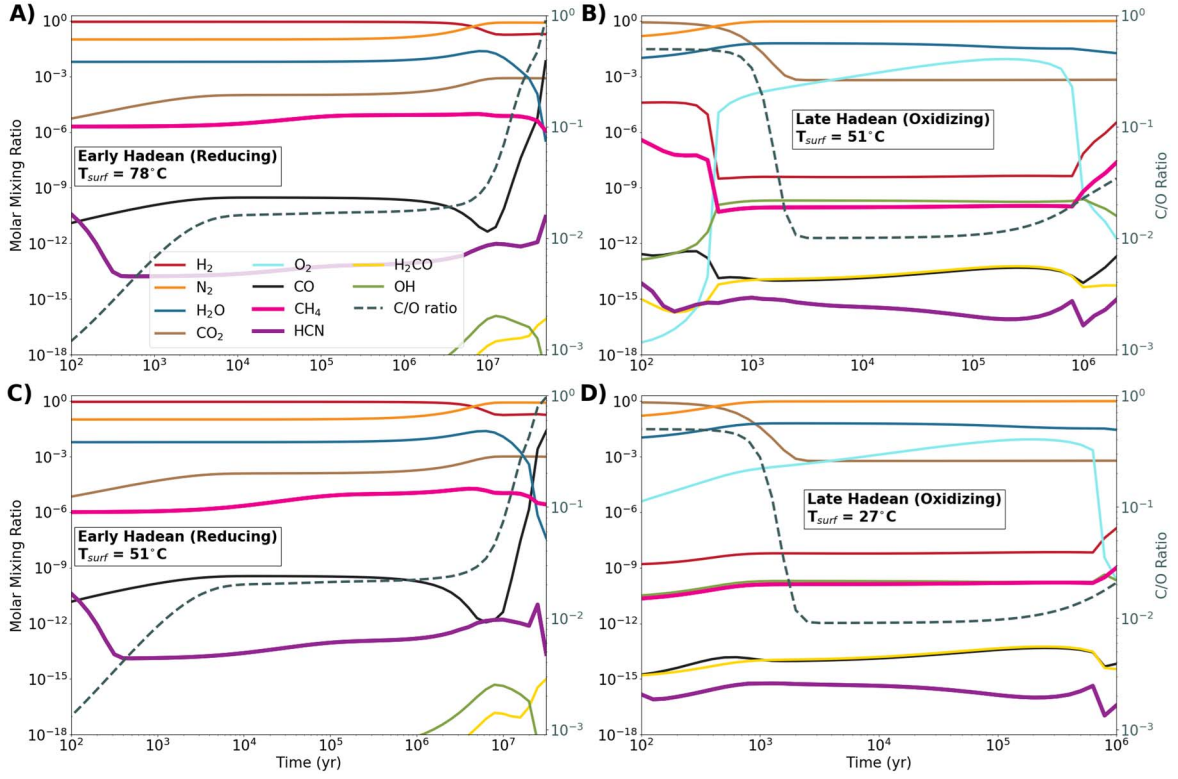


Figure 3. Abundances of key species in the lowest atmospheric layer as a function of time in our four early Earth models. The evolving C/O ratio in the surface layer is the dotted line with values labeled on the right-hand y-axis. Model details are in Table 1.

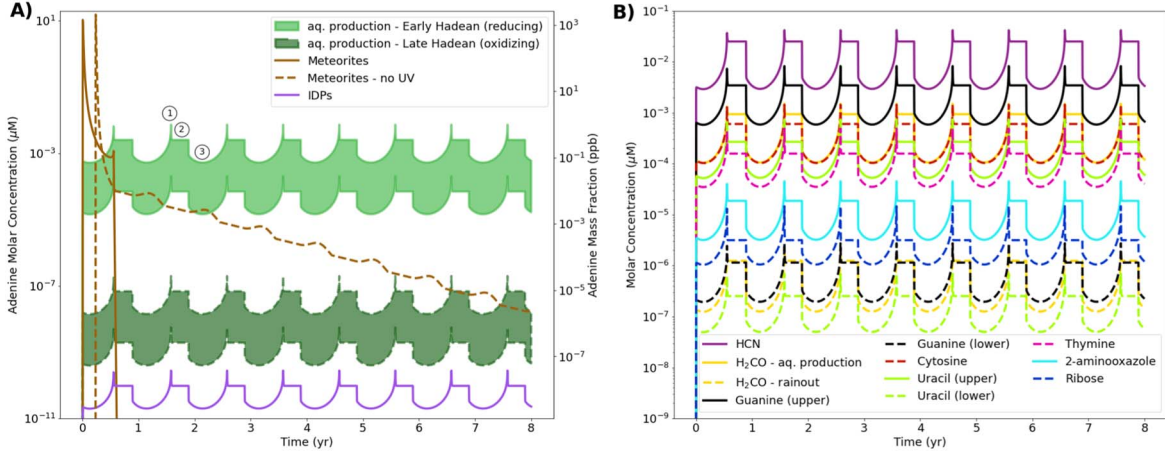


Figure 4. A) Comparative histories of adenine concentrations in warm little ponds from aqueous production (this work), versus delivery from meteorites and interplanetary dust particles (IDPs) (Pearce et al. 2017). Concentrations are calculated using the sources and sinks pond model developed in Pearce et al. (2017) that cycles between ~6 months of wet and ~6 months of dry conditions; the one exception is the “Meteorites - no UV” model, which is calculated for a pond that never dries up and for which UV is never turned on. Aqueous production of adenine is sourced from atmospheric rain-out of HCN multiplied by the range of experimental yields (see Table A6). Sinks include UV photodissociation in the dry phase, and hydrolysis and seepage in the wet phase. At location (1), the pond has dried down to 1 mm, creating the maximum concentration. At location (2), UV irradiation is turned on and the concentration reduces until production from HCN influx and destruction from UV dissociation equilibrate. Finally, at location (3), precipitation has filled the pond up to its highest point, resulting in the concentration minimum. This cycle repeats annually. Hydrolysis has no effect on these curves, as the other two sinks are more efficient and occur on shorter timescales. The meteorite and IDP curves are taken directly from Pearce et al. (2017). (B) Calculations of pond concentrations of various biomolecules as a result of atmospheric rain-out of HCN or H₂CO (yellow dotted line) for our early Hadean (reducing) model A. See Table A6 for the experimental yields and sink rates used in the model calculations.

rain-out (influx) rates from our early Hadean (reducing) and late Hadean (oxidizing) atmospheric models (see Figure B1 for rain-out rates). Adenine concentrations are displayed as shaded regions to cover the range of experimental yields of adenine production from HCN. We also display for comparison the concentrations of adenine from meteoritic and interplanetary

dust particle (IDP) delivery calculated using the same source/sink pond models in Pearce et al. (2017).

Given the range of experimental conditions, there are additional uncertainties beyond the shaded regions that are not displayed here. Aqueously produced biomolecule concentrations could be lower than the abundances calculated here due

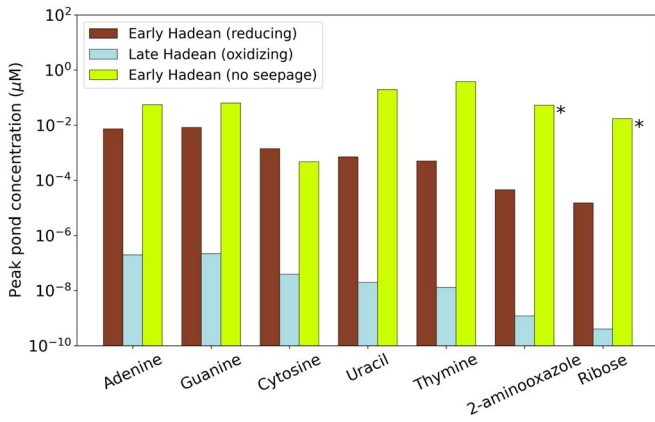


Figure 5. Peak concentrations of biomolecules produced in situ in our WLP models (see Table B1 for more details). *Hydrolysis rates are not estimated for 2-aminooxazole and ribose, therefore concentrations should be considered as maximum values in the absence of aqueous chemical sinks.

to (1) the low nanomolar-range HCN pond concentrations compared to typically molar-range experimental concentrations, (2) differences in the radiation field used in experiments for photolytic H_2CO production versus the solar radiation incident on WLPs, and (3) uncertainties in the hydrolysis and photodestruction rates for each biomolecule. Conversely, biomolecule concentrations could be higher than our calculated values due to various concentration mechanisms including adsorption to mineral surfaces, and sequestration into mineral gels or amphiphilic matrices (Damer & Deamer 2020; Deamer 2017). Given these uncertainties, we present the following biomolecule concentrations as an upper bound in the absence of concentration mechanisms.

Adenine concentrations from aqueous production peak at 7.3 nM (1 ppb) and 0.2 pM (0.03 ppb) for our early Hadean (reducing) and late Hadean (oxidizing) models, respectively. The early Hadean (reducing) adenine concentrations are approximately three orders of magnitude smaller than the peak adenine concentration from meteoritic delivery of $10.6 \mu\text{M}$ (1.43 ppm); however, the adenine concentration from aqueous production can be sustained for more than 100 million years rather than days.

Adenine concentrations from delivery by IDPs are the most dilute in our WLP models, peaking at $\sim 10^{-10} \mu\text{M}$ (Pearce et al. 2017).

In Figure 4(B), we plot the pond concentrations of HCN and H_2CO from atmospheric rain-out, as well as the concentrations of nucleobases, ribose, H_2CO , and 2-aminooxazole from aqueous HCN-based production. HCN concentrations peak at $0.04 \mu\text{M}$ and reduce to approximately 3 nM when the water level in the pond is highest.

We learn from these models that formaldehyde in WLPs likely did not come directly from the atmosphere during the early Hadean. H_2CO concentrations from aqueous photolytic production peak at 1.5 nM, which is 3–4 orders of magnitude higher than the maximum H_2CO concentration from atmospheric rain-out (4.1×10^{-5} nM). On the other hand, for our late Hadean (oxidizing) model B, the H_2CO concentration from rain-out is 0.34 nM, which is two orders of magnitude higher than the H_2CO concentration from photolytic production. Therefore, in oxidizing conditions H_2CO in WLPs may also come directly from the atmosphere.

Our model solves another main limitation of meteorites as a source of prebiotic nucleobases, in that cytosine and thymine are not present in meteorites (Callahan et al. 2011; Pearce & Pudritz 2015, 2016). During the early Hadean, guanine, cytosine, uracil, and thymine concentrations peak at 8.2, 1.4, 0.7, and 0.5 nM, respectively. 2-aminooxazole and ribose concentrations peak at 0.045 and 0.015 nM, respectively. Meteorites would have provided brief (\sim a few weeks) enhancements in nucleobase concentrations up to three orders of magnitude above the base abundance from in situ production.

In Figure 5 and Table B1, we summarize the peak concentrations of key biomolecules and biomolecule precursors in our model WLPs for our early Hadean (reducing) and late Hadean (oxidizing) models A and B. We also include the early Hadean (reducing) model A with seepage turned off, representing a scenario where biomolecules are not exposed to this sink due to blockage of rock pores by amphiphilic multilamellar matrices or mineral gels, or adsorption onto mineral surfaces. Concentrations of biomolecules from the early Hadean (reducing) model A are approximately four orders of magnitude higher than concentrations from the late Hadean (oxidizing) model B. When seepage is turned off, biomolecule concentrations increase in model A to ~ 1 –400 nM. It is interesting to note that there are order-of-magnitude differences in the concentrations of purine nucleobases (adenine and guanine) versus the pyrimidine nucleobases (cytosine, uracil, and thymine). Does this have implications for the frequencies of various bases in the first replicating RNA polymers?

4. Discussion

4.1. Comparison with Other Methods and Experiments

We have developed multiple new methods that have greatly enhanced the capabilities of nonequilibrium calculations of atmospheric HCN on early Earth. These include the calculation of composition-dependent pressure–temperature (P – T) profiles using a radiative transfer code, the inclusion of lightning chemistry, and the time-dependent influx of H_2 , CO_2 , and CH_4 from impact degassing, volcanism, and oceanic geochemistry, respectively.

Past nonequilibrium atmospheric models for the Archean (~ 3.8 –2.5 bya) have computed HCN production for a range of CH_4 , H_2 , and CO_2 abundances using a commonly suggested input P – T profile for early Earth with surface temperatures of 273–288 K (Zahnle 1986; Tian et al. 2011). These models imposed CH_4 abundances in the 10–1000 ppm range, either did not fix H_2 or imposed H_2 abundances in the 0.01%–1% range, and imposed CO_2 abundances in the 0.04%–3% range. Our strategy is different, as we begin with initial reducing (4.4 bya) or oxidizing (4.0 bya) conditions that are thought to represent each epoch, and calculate the composition-dependent input P – T profiles using a radiative transfer code. As a result, our surface temperatures are 27°C – 78°C hotter than these past Archean models. Then, we allow the concentrations of all species to evolve over time based on their source and sink rates at each epoch.

For example, CO_2 reaches a steady surface abundance of $\sim 0.05\%$ – 0.1% in our models based on the source rates from volcanic outgassing and association chemistry balanced with the sink rates from atmospheric rain-out and photodissociation.

Our steady-state abundances are similar to the lower end of CO₂ abundances from past Archean models. Similarly, our end-of-simulation H₂ abundances (18%–19% and ppb–ppm for reducing and oxidizing models, respectively) are balanced by the source rate from epoch-dependent impact bombardment, and the sink rates from hydrodynamic escape, photodissociation, and chemistry. The steady-state H₂ abundances in our reducing models are at least an order of magnitude higher than those calculated or imposed in the Archean models, while the steady-state H₂ abundances in our oxidizing models are at least two orders of magnitude lower than the values calculated or imposed in those models.

CH₄ abundances are based on source rates from oceanic sources balanced with sink rates from photodissociation and chemistry. Surface CH₄ abundances reach end-of-simulation values that are 0–4 orders of magnitude lower than the range of CH₄ concentrations imposed in the past Archean models. Given the correlation between HCN production and CH₄ abundance, our calculated surface HCN concentrations tend to be lower than those calculated in these Archean models. The Archean models compute HCN mixing ratios near the surface to be $\sim 10^{-12}$ – 10^{-7} . The lower end of this range is similar to the surface HCN abundances in our reducing 4.4 bya models of $\sim 10^{-11}$, but three orders of magnitude higher than the HCN mixing ratios in our oxidizing 4.0 bya models of $\sim 10^{-15}$ after ~ 1 Myr. This three-orders-of-magnitude discrepancy is due to the fact that our 4.0 bya models are more oxidizing than the previous Archean models. In other words, our 4.0 bya models contain higher concentrations of oxygen species such as O₂ and H₂O, and lower concentrations of reducing gases such as H₂ and CH₄.

Zahnle et al. (2020) modeled nonequilibrium chemistry following a large-body impact with input P – T profiles based on a simple analytic equation for a moist adiabat. These models began with concentrations of H₂, CO, CO₂, CH₄, and NH₃ that result from various impactors equilibrating with different mineral redox buffers. They found that impactors of at least the size of Vesta (525 km) are required to sustain the high temperatures required for rapid methane production. These models produced post-impact atmospheric CH₄ abundances of $\sim 3\%$, which resulted in similarly high (\sim a few %) HCN abundances for a few million years after impact. These post-impact CH₄ abundances are four orders of magnitude higher than the ppm-range steady-state CH₄ abundances from our reducing models. The analytic equation Zahnle et al. (2020) used for obtaining a habitable surface and P – T profile for their nonequilibrium chemistry models does not consider the strength of various opacity sources such as H₂–H₂ collisionally induced absorption (CIA) and CH₄. Zahnle et al. (2020) compute surface temperatures of ~ 320 K for a post-Vesta-impact atmosphere of 3.9 bar of H₂ and 0.17 bar of CH₄. We are unable to obtain habitable surfaces when modeling H₂ atmospheres >2 bar using the equations of radiative transfer. In our radiative transfer models, we find H₂–H₂ CIA produces a strong greenhouse effect above ~ 1.13 bar of H₂. The surface temperature of our early Hadean (reducing) model A, which has 1.5 bar of H₂, 2 ppm of CH₄, and ppm-range H₂O, is reaching the limits of habitability at 78°C. This suggests that the resultant high atmospheric pressures of H₂ and CH₄ from the large-body impacts modeled by Zahnle et al. (2020) would produce atmospheric temperatures too high for WLPs to exist. More research needs to be done to understand whether a large-

body impact could provide high HCN rain-out rates to WLPs after a substantial amount of H₂ escapes from the upper atmosphere, allowing the surface to cool to habitable temperatures.

Atmospheric models of nitrogen-rich rocky exoplanets that use C/O ratio as an adjustable parameter produce HCN mixing ratios of 10^{-8} – 10^{-7} for atmospheric C/O ratios near 0.5, and HCN mixing ratios of $\sim 10^{-3}$ for C/O ratios >1.5 (Rimmer & Rugheimer 2019). We do not use C/O as an adjustable parameter, because we find that the balance of outgassing and losses of species such as CO₂, H₂O, and CH₄ in our models leads to surface C/O ratios that vary from ~ 0.001 to 1 over the course of the simulations. These C/O ratios are generally lower than those explored by Rimmer & Rugheimer (2019).

Pinto et al. (1980) modeled the chemical kinetics of formaldehyde production in a primitive Earth atmosphere composed of N₂, H₂O, CO₂, CO, and H₂. They employed a highly reduced network of eight photochemical reactions and 31 neutral reactions between 13 species. Their computed formaldehyde rain-out rates ($\sim 10^{11}$ mol yr^{−1}) are approximately three orders of magnitude higher than our maximum formaldehyde rain-out rates for Model B ($\sim 10^8$ mol yr^{−1}). Part of this discrepancy is due to the higher efficiency of their H₂CO rain-out. They used a rain-out (scavenging) coefficient (cm³ s^{−1}) that is based on H₂CO rain-out on Earth today, whereas we compute rain-out using a deposition velocity (cm s^{−1}) that is calculated from a thin-film parameterization model (Wagner et al. 2002) and is used in more recent atmospheric models that follow the treatment of deposition velocity (Ranjana et al. 2020; Hu et al. 2012). The treatment used in Pinto et al. (1980) produces an H₂CO rain-out rate that is about a factor of 20 greater than our models would produce if we had the same surface H₂CO density. Considering these differences, we may be underestimating H₂CO rain-out by up to a factor of ~ 20 . However, the main source of discrepancy is because their atmosphere is more oxidizing than all of our models. They do not include CH₄ or other reduced carbon species (e.g., C₂H₂, C₂H₆) in their network, which, if given initial abundances, would change the oxidation state of the atmosphere and decrease the production of oxidized carbon species such as H₂CO.

Miller–Urey experiments have shown that reducing conditions are more favorable than oxidizing conditions for biomolecule production (Schlesinger & Miller 1983; Cleaves et al. 2008). For example, Schlesinger & Miller (1983) found a difference of ~ 3 – 4 orders of magnitude in amino acid yields when switching from reducing (H₂-dominant) to oxidizing (CO₂-dominant) experimental conditions. This is consistent with our results, where we have shown that the early reducing phase of the Hadean eon at 4.4 bya produces atmospheric HCN and RNA building blocks ~ 4 orders of magnitude higher in concentration than during the late oxidizing phase at 4.0 bya. Some Miller–Urey experiments have shown reasonable success in amino acid production in CO₂/N₂ conditions when buffering the solution with calcium carbonate (Cleaves et al. 2008); however, this is likely demonstrating catalytic effects that increase amino acid production yields from low HCN concentrations.

4.2. Biomolecule Concentrations

Of critical importance is how high pond concentrations of biomolecules such as nucleobases, ribose, and 2-aminooxazole

would need to be in order for nucleotide synthesis and subsequent RNA polymerization to occur. Published laboratory experiments that react nucleobases to produce nucleosides and nucleotides typically use 400 μM –100 mM concentrations of nucleobases and obtain 0.01%–74% yields (Ponnamperuma et al. 1963; Fuller et al. 1972; Saladino et al. 2017; Nam et al. 2018). The lowest end of this experimental concentration range is three orders of magnitude higher than the maximum nucleobase concentrations from our early Hadean (4.4 bya) model without seepage (~ 400 nM). Mechanisms to increase nucleobase concentrations in WLPs would likely be necessary given that experiments at nanomolar concentrations to produce nucleotides and RNA have not been reported, and achieving high yields requires optimal conditions. Such mechanisms include adsorption to mineral surfaces, and sequestration into amphiphilic multilamellar matrices or mineral gels (Damer & Deamer 2020; Deamer 2017).

The porosity of WLPs is difficult to assess. While something is known about the porosity of volcanic basalts (Hamouda et al. 2014), pond environments are likely to be messier affairs. Various kinds of debris and films would be expected to accumulate at the bottom of ponds, such as amphiphilic multilamellar matrices or mineral gels. These would clog the pores, reducing losses due to seepage. It is difficult to estimate how large this effect would be. We can, however, estimate an upper limit to abundances of biomolecules by computing models for which seepage is set to zero. Turning off seepage in our models provides an increase in nucleobase concentrations by 1–3 orders of magnitude after 500–10,000 yr (see Figure B3). In this scenario, hydrolysis takes over as the main concentration-limiting sink.

Ribose and 2-aminooxazole in our models are the most dilute of the RNA building blocks, with concentrations in the sub-nanomolar range. Again, laboratory experiments use much higher concentrations than this for nucleotide synthesis, typically in the millimolar to molar range (Ponnamperuma et al. 1963; Fuller et al. 1972; Nam et al. 2018; Powner et al. 2009). Saladino et al. (2017) used only 8 μM ribose to produce nucleosides in a neat formamide solution; however, because this experiment was performed with a different solvent, it is unclear whether similar results could occur in aqueous solution. Our results encourage additional experimental work to determine the levels that are sufficient for nucleotide synthesis in realistic prebiotic conditions.

5. Conclusion

Our comprehensive treatment of the early Earth’s coupled atmosphere–impactor–ocean system reveals several striking insights. It is the initial high rate of H_2 impact degassing soon after the Moon-forming impact with the Earth that keeps its atmosphere in a chemically reducing state. Photochemistry-dominated HCN formation from methane in the lower atmosphere rains out into WLPs steadily over about a hundred million years. There, aqueous chemistry continuously drives nucleobase and perhaps nucleotide precursor synthesis to levels where polymerization by condensation reactions can occur. Overall, this steady input totally dominates that which is possible from more isolated meteoritic infall events. With a declining bombardment throughout the Hadean eon (Chyba 1990; Pearce et al. 2017), the transition from reducing to oxidizing atmospheric conditions is roughly linear from 4.4 to 4.0 bya. After 4.3 bya, the reducing conditions dissipate.

This terminates new biomolecular formation so that RNA-based life would have already had to appear. The astrophysical and chemical processes we model are quite general. They are intrinsic to the late phases of terrestrial planet formation, anywhere. This suggests that life on Earth, and perhaps also on other Earth-like worlds, began in the chaotic conditions that prevailed soon after their formation.

We thank the anonymous referee whose comments and questions led to improvements in this work. We thank David Catling for his critical analysis of an early draft of this paper and Nick Wogan for catching an error in our pre-published calculations. We thank Steve Benner, Jeffrey Bada, David Deamer, Bruce Damer, Oliver Trapp, Paul Higgs, Greg Slater, and Paul Rimmer for interesting discussions regarding this work. This research is part of a collaboration between the Origins Institute at McMaster University and the Heidelberg Initiative for the Origins of Life. The research of B.K.D.P. was supported by an NSERC Alexander Graham Bell Canada Graduate Scholarship-Doctoral (CGS-D) and Ontario Graduate Scholarship. K.M. was supported by the Excellence Cluster ORIGINS which is funded by the Deutsche Forschungsgemeinschaft (DFG, German Research Foundation) under Germany’s Excellence Strategy—EXC-2094-390783311. R.E.P. is supported by an NSERC Discovery Grant. T.H. acknowledges support from the European Research Council under the Horizon 2020 Framework Program via the ERC Advanced Grant Origins 83 24 28. We acknowledge Compute Canada for allocating the computer time required for this research. We thank Steve Janzen at McMaster Media Resources for his superb work in rendering Figure 1.

Author Contributions: B.K.D.P., K.M., R.E.P., and T.H. designed research; B.K.D.P. performed research; K.M. performed atmospheric chemistry simulations; B.K.D.P. performed numerical pond simulations; K.E.C. and B.K.D.P. performed P – T profile simulations; B.K.D.P. and R.E.P. analyzed data; and B.K.D.P., R.E.P., and T.H. wrote the paper.

Competing Interests: No competing financial interests exist.

Appendix A Supplementary Methods

A.1. Atmospheric Simulations

Self-consistent disequilibrium atmospheric simulations are carried out iteratively using the consistent reduced atmospheric hybrid chemical network oxygen extension (CRAHCN-O) (Pearce et al. 2020a, 2020b) coupled with a 1D chemical kinetic model (ChemKM) (Molaverdikhani et al. 2019a, 2020a), with input pressure–temperature (P – T) structures calculated using petitRADTRANS (Mollière et al. 2019).

CRAHCN-O now contains 259 one-, two-, and three-body reactions, whose rate coefficients are gathered from experiments when available ($\sim 40\%$), and are otherwise calculated using accurate, consistent, theoretical quantum methods ($\sim 60\%$). Approximately 93 of the reactions in CRAHCN-O were missing from the literature prior to their discovery in Pearce et al. (2019, 2020a, 2020b). This network can be used to calculate HCN and H_2CO chemistry in atmospheres characterized by any of N_2 , CO_2 , CH_4 , H_2O , and H_2 . We added 28 new reactions to CRAHCN-O after our preliminary simulations showed the artificial buildup of species that previously had no

Table A1
New Two-body Reactions Added to CRAHCN-O for Our Early Earth Atmospheric Models, and Their Experimental Arrhenius Coefficients

Reaction Equation	α	β	γ	Source(s)
$\text{HCCO} + \text{NO} \rightarrow \text{HCNO} + \text{CO}$	1.4×10^{-11}	0	-320	Carl et al. (2000)
$\text{HCCO} + \text{NO} \rightarrow \text{HCN} + \text{CO}_2$	6.1×10^{-12}	-0.72	-200	Carl et al. (2000)
$\text{HCCO} + {}^3\text{O} \rightarrow \text{CO} + \text{CO} + \text{H}$	1.6×10^{-10}	0	0	Baulch et al. (1992)
$\text{HCCO} + \text{H} \rightarrow \text{CO} + {}^3\text{CH}_2$	2.1×10^{-10}	0	0	Glass et al. (2000); Frank et al. (1988)
$\text{NCO} + \text{O}_2 \rightarrow \text{CO}_2 + \text{NO}$	1.3×10^{-12}	0	0	Schacke et al. (1974)
$\text{NCO} + \text{NO} \rightarrow \text{N}_2 + \text{CO}_2$	1.6×10^{-11}	0	0	Cooper et al. (1993); Cooper & Hershberger (1992)
$\text{NCO} + {}^3\text{O} \rightarrow \text{NO} + \text{CO}$	6.4×10^{-11}	-1.14	0	Becker et al. (2000)
$\text{NCO} + \text{H} \rightarrow \text{NH} + \text{CO}$	2.2×10^{-11}	0	0	Becker et al. (2000)
$\text{HO}_2 + {}^3\text{O} \rightarrow \text{O}_2 + \text{OH}$	5.4×10^{-11}	0	0	Baulch et al. (1992)
$\text{HO}_2 + \text{OH} \rightarrow \text{H}_2\text{O} + \text{O}_2$	4.8×10^{-11}	0	-250	Baulch et al. (1992)
$\text{HO}_2 + \text{H} \rightarrow \text{H}_2\text{O} + {}^3\text{O}$	5.0×10^{-11}	0	866	Baulch et al. (1992)
$\text{HO}_2 + \text{H} \rightarrow \text{O}_2 + \text{H}_2$	7.1×10^{-11}	0	710	Baulch et al. (1992)
$\text{HO}_2 + \text{H} \rightarrow \text{OH} + \text{OH}$	2.8×10^{-10}	0	440	Baulch et al. (1992)
$\text{O}_2 + \text{HCO} \rightarrow \text{CO} + \text{HO}_2$	8.5×10^{-11}	0	850	Tsang & Hampson (1986)
$\text{O}_2 + \text{C}_2\text{H} \rightarrow \text{HCCO} + {}^3\text{O}$	1.0×10^{-12}	0	0	Tsang & Hampson (1986)
$\text{O}_2 + \text{C}_2\text{H} \rightarrow \text{HCO} + \text{CO}$	4.0×10^{-12}	0	0	Tsang & Hampson (1986)
$\text{O}_2 + \text{CN} \rightarrow \text{NCO} + {}^3\text{O}$	1.1×10^{-11}	0	-205	Baulch et al. (1992)
$\text{O}_2 + {}^3\text{N} \rightarrow \text{NO} + {}^3\text{O}$	4.5×10^{-12}	1.0	3720	Baulch et al. (1994)
$\text{O}_2 + \text{CH} \rightarrow \text{OH} + \text{CO}$	5.0×10^{-11}	0	0	Lichtin et al. (1984, 1983)
$\text{O}_2 + \text{C} \rightarrow \text{CO} + {}^3\text{O}$	3.0×10^{-11}	0	0	Duncanson & Guillory (1983); Messing et al. (1979) Geppert et al. (2000); Dorthé et al. (1991) Becker et al. (1988); Husain & Young (1975) Husain & Kirsch (1971); Braun et al. (1969) Martinotti et al. (1968) Atkinson et al. (1989)
$\text{NO} + {}^4\text{N} \rightarrow \text{N}_2 + {}^3\text{O}$	3.1×10^{-11}	0	0	Herron (1999)
$\text{NO} + {}^2\text{N} \rightarrow \text{N}_2 + {}^3\text{O}$	6.0×10^{-11}	0	0	Baulch et al. (1994)
$\text{NO} + \text{C} \rightarrow \text{CN} + {}^3\text{O}$	2.5×10^{-11}	0	0	Tsang & Hampson (1986)
$\text{C}_2\text{H} + \text{CH}_4 \rightarrow \text{C}_2\text{H}_2 + \text{CH}_3$	3.0×10^{-12}	0	250	Baulch et al. (1992)
$\text{C}_2\text{H} + {}^3\text{O} \rightarrow \text{OH} + \text{CO}$	1.7×10^{-11}	0	0	

Note. These are the most efficient sink reactions for species that would otherwise erroneously build up over timescales of tens to hundreds of millions of years. The Arrhenius expression is $k(T) = \alpha(T/300 \text{ K})^\beta e^{-\gamma/T}$.

Table A2
New Three-body Reactions Added to CRAHCN-O for Our Early Earth Atmospheric Models, and Their Calculated or Experimental Lindemann Coefficients

Reaction Equation	$k_\infty(298)$	$k_0(298)$	Source(s)
$\text{O}_2 + \text{H} + \text{M} \rightarrow \text{HO}_2 + \text{M}$	7.5×10^{-11}	(M = N ₂) $3.9 \times 10^{-30} T^{-0.8}$ (CO ₂) $5.8 \times 10^{-30} T^{-0.8}$ (H ₂) $4.3 \times 10^{-30} T^{-0.8}$	(N ₂) Baulch et al. (1992) (H ₂ O) Baulch et al. (1992) (H ₂) Baulch et al. (1992)
$\text{C}_2\text{H} + \text{H} + \text{M} \rightarrow \text{C}_2\text{H}_2 + \text{M}$	2.3×10^{-11}	(M = N ₂) 5.8×10^{-28} (CO ₂) 7.1×10^{-28} (H ₂) 4.2×10^{-28}	This work
$\text{C} + \text{H}_2 + \text{M} \rightarrow {}^3\text{CH}_2 + \text{M}$	1.6×10^{-9}	(M = N ₂) 7.0×10^{-32} (CO ₂) 7.0×10^{-32} (H ₂) 7.0×10^{-32}	This work, Husain & Young (1975), Husain & Kirsch (1971)

Note. These are the most efficient high-pressure sink reactions for species that would otherwise erroneously build up over timescales of tens to hundreds of millions of years. Experimental rate coefficients are listed when available, otherwise we calculate them using canonical variational transition state theory and Rice–Ramsperger–Kassel–Marcus master equation theory with the BHandHLYP density functional and the aug-cc-pVDZ basis set (see Pearce et al. 2020a, 2020b for details on how these calculations are performed). k_∞ is the second-order rate coefficient in the high-pressure limit with units cm³ s⁻¹. k_0 is the third-order rate coefficient in the low-pressure limit with units cm⁶ s⁻¹. These values fit into the pressure-dependent rate coefficient equation $k = \frac{k_0[\text{M}] / k_\infty}{1 + k_0[\text{M}] / k_\infty} k_\infty$.

reaction sinks. We list the new two-body and three-body reactions in Tables A1 and A2, respectively.

All values are experimental, except for the low- and high-pressure limit rate coefficients for $\text{C}_2\text{H} + \text{H} + \text{M} \rightarrow \text{C}_2\text{H}_2 + \text{M}$ and the high-pressure limit rate coefficient for $\text{C} + \text{H}_2 + \text{M} \rightarrow {}^3\text{CH}_2 + \text{M}$, as there were no experimental values available. For these reactions, we calculate the rate coefficients

using the same validated theoretical and computational quantum methods developed in Pearce et al. (2020a, 2020b) for the other three-body reactions in CRAHCN-O.

The ChemKM code takes as input: (a) a chemical network, (b) an atmospheric P – T structure, (c) an eddy diffusion profile to characterize turbulent mixing, (d) the solar radiation spectrum at the top-of-atmosphere (TOA), (e) wavelength-

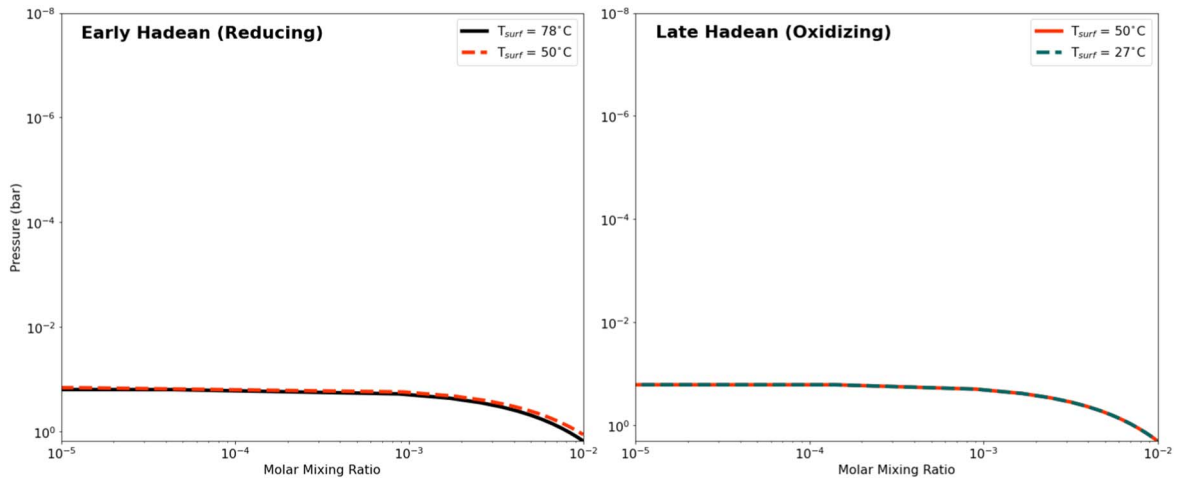


Figure A1. Initial tropospheric water vapor profiles for our four early Earth models.

dependent photochemical reactions, and (f) incoming and outgoing molecular fluxes from the surface and TOA (i.e., impact degassing, volcanic outgassing, rain-out, hydrogen escape, and chemical production from lightning). ChemKM uses the plane-parallel two-stream approximation to calculate radiative transfer, and includes both photoabsorption and Rayleigh scattering. The pressure profiles remain static throughout the simulations; therefore we must assume that pressure has reached equilibrium with the influx and outflux of atmospheric gases. This assumption is valid for our models, as our H_2 impact degassing rates never exceed the H_2 escape rates.

P - T structures for early Earth models are calculated using the petitRADTRANS software package (Mollière et al. 2019). petitRADTRANS is a 1D radiative transfer code that uses the Guillot analytic temperature model (Guillot 2010) and correlated- k opacity tables to solve for atmospheric temperatures of planets with no surface boundary condition. Visible opacities are calculated using the Planck mean, and infrared opacities are calculated using the Rosseland mean (Parmentier & Guillot 2014). Our models are all 100 layers, from surface pressures of ~ 1 –2 bar to TOA pressures of 1×10^{-8} bar. We implement cloudless and hazeless models given the large uncertainties of these parameters for the early atmosphere. We note that the lack of biogenic cloud condensation nuclei would have led to a shorter lifetime for optically thick convective clouds during the Hadean (Rosing et al. 2010), reducing their contribution to both the greenhouse and albedo when compared with those of modern Earth (Charnay et al. 2020).

In Figure A1 we display the initial water vapor profiles in the troposphere of our four early Earth models. We make an incremental improvement over the standard water vapor profile of Manabe & Wetherald (1967) for Earth’s atmosphere by calculating tropospheric water abundances in two steps. In the first step, we iterate the Arden Buck equation (Buck 1981), which is dependent on temperature, and the P - T calculations from petitRADTRANS, which are dependent on water composition. To avoid a runaway greenhouse due to water vapor feedback, we parameterize the strength of water vapor feedback by decreasing the relative humidity (RH) by $\beta = 6\%$ for every 1°C of warming (Held & Soden 2000). In step two, we smooth out these profiles to avoid numerical instabilities in ChemKM. We use the calculated water vapor at the tropopause and linearly increase the mixing ratio moving downwards in altitude to reach a typical water vapor abundance of 1% for wet

rocky planets (Hu et al. 2012). The tropopause is chosen to be 0.14 bar, similar to the present-day Earth (Robinson & Catling 2014).

The three main inputs for our P - T structure calculations are (a) input composition, (b) equilibrium temperature (T_{eq}), and (c) internal temperature (T_{int}). Initial guesses for input compositions were selected to represent reducing (H_2/N_2 -dominant) or oxidizing (CO_2/N_2 -dominant) phases of the early (4.4 bya) and late (4.0 bya) Hadean eon. Surface pressure and methane abundance are adjusted from 1 to 2 bar and 1 to 10 ppm, respectively, to maintain habitable surface temperatures (i.e., $0^\circ\text{C} \leq T_s \leq 100^\circ\text{C}$) (see Table 1). Equilibrium temperatures are calculated using the equation

$$T_{\text{eq}} = \left(\frac{(1 - A)L_\odot}{16\pi\sigma a^2} \right)^{1/4}, \quad (\text{A1})$$

where T_{eq} is equilibrium temperature, A is albedo, L_\odot is solar luminosity, σ is the Stefan–Boltzmann constant, and a is the semimajor axis of the planet.

Luminosities for the Sun at 4.4 bya ($0.705 L_\odot$) and 4.0 bya ($0.728 L_\odot$) are obtained from a precomputed stellar evolution model of a Sun-like star (Heller et al. 2020; Baraffe et al. 2015). The Hadean Earth would have been mostly covered in water; therefore, albedo is taken to be 0.06, which is consistent with a cloudless water world (Roesch et al. 2002).

Internal heat flow is taken to be three times the present value, which is compatible with thermal modeling of the Hadean (Sleep 2010). Using the Stefan–Boltzmann law, this results in internal temperatures of $T_{\text{int}} = 43.3$ K.

In Figure A2, we display the P - T profiles for our four Hadean models.

In Figure A3, we display the eddy diffusion profile used for all our early Earth models. This is the standard profile for early Earth and analogous exoplanets (Ranjan et al. 2020; Arney et al. 2016; Tian et al. 2011; Zahnle 1986).

The TOA radiation for our models is based on the solar mean (Thuillier et al. 2004) with a solar zenith angle of 50° ; however, we increase the UV flux to simulate the increased activity of the young Sun. In Table A3, we display the multiplicative factors used in our models for each UV wavelength interval. Values are based on observations of young solar analogs (ages ~ 0.1 –7 Gyr) (Ribas et al. 2005).

Our 33 photochemical reactions mostly match those from the Titan models by Hébrard et al. (2012); however, we update the

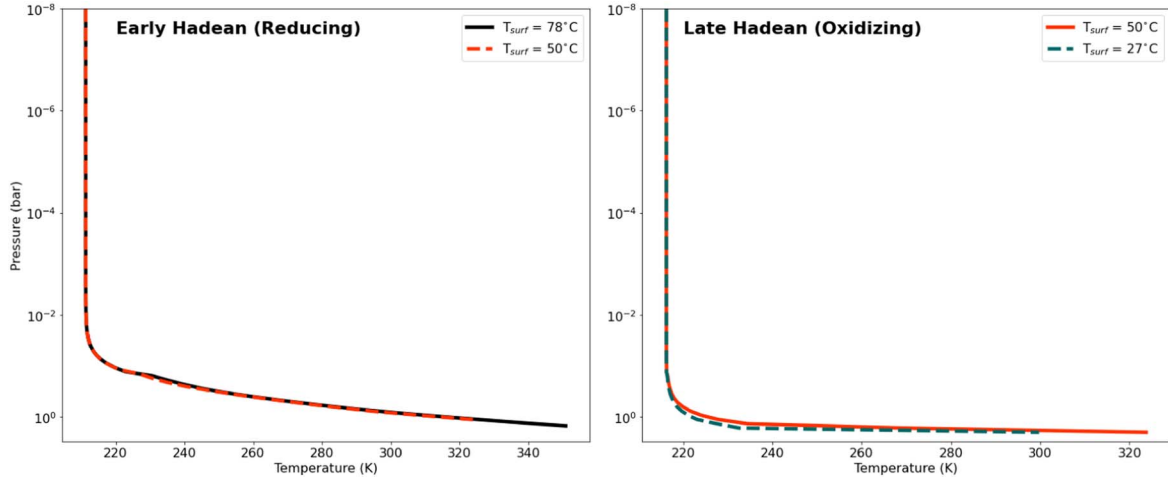


Figure A2. Pressure–temperature profiles for our four early Earth models, calculated with petitRADTRANS using the input compositions displayed in Table 1.

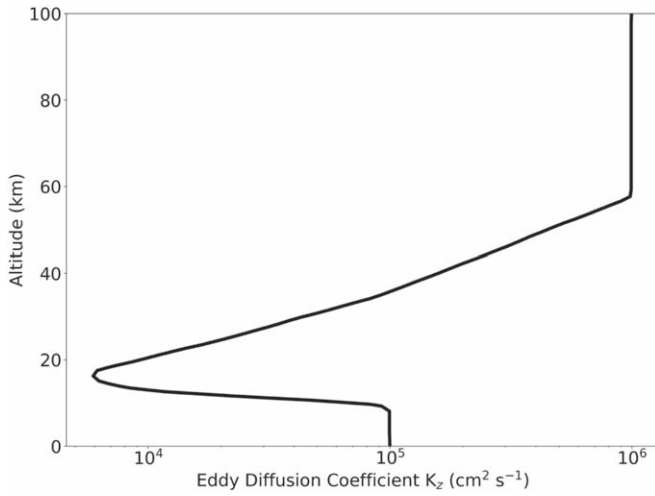


Figure A3. Eddy diffusion profile for all early Earth models, characterizing turbulent mixing in the atmosphere. This is the standard K_z profile used for atmospheric simulations of early Earth and analogous exoplanets (Ranjan et al. 2020; Arney et al. 2016; Tian et al. 2011; Zahnle 1986).

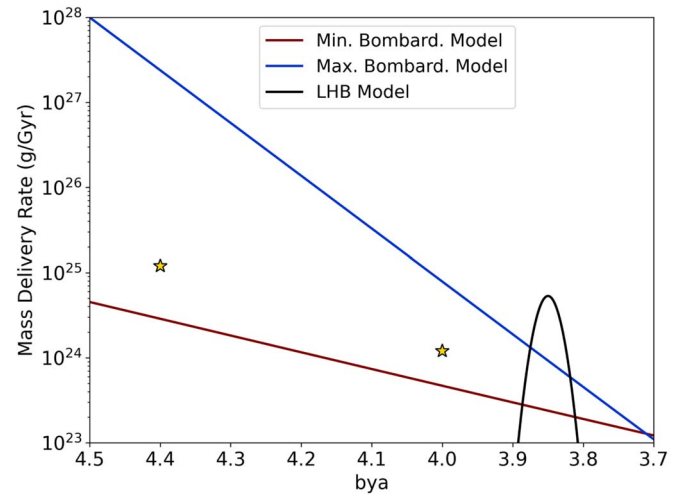


Figure A4. Three early Earth bombardment models from Pearce et al. (2017) based on fits to the lunar cratering record. The gold stars represent the bombardment rates we used to calculate H_2 impact degassing for our 4.4 and 4.0 bya atmospheric models.

Table A3

Multiplicative Increase in UV Irradiation from Present-day Values Based on Observations of Young Solar Analogs (Ribas et al. 2005)

Model	1–20 Å	20–360 Å	360–920 Å	920–1200 Å
4.0 bya	60	10	9	7
4.4 bya	500	60	30	20

H_2O absorption cross sections with the recent near-UV experimental measurements from Ranjan et al. (2020), we remove erroneous CO_2 absorption below 202 nm (Ranjan et al. 2020), and we add photochemistry for O_2 and HO_2 following treatments in Hu et al. (2012) and CH_3OH using experimental cross sections from Lange et al. (2020) and Burton et al. (1992).

We couple planetary surface processes to our atmospheric models by adding influxes of species to the lowest layer of our atmospheres. These include H_2 impact degassing, CO_2 outgassing from volcanoes, CH_4 outgassing from hydrothermal systems, H_2O evaporation from the ocean, and chemical production (e.g., HCN, CO, 3O , H) due to lightning.

Equilibrium chemistry calculations performed by Zahnle et al. (2020) for enstatite chondrite impactors suggest that H_2 degassing via the reaction $Fe + H_2O \rightarrow FeO + H_2$ scales linearly with impactor mass, at a rate of $\sim 10^{-21}$ mol H_2 cm^{-2} g^{-1} impactor. Mathematical fits to the lunar cratering record provide us with an estimate of the rate of impactors on early Earth at a given epoch. In Figure A4, we display our model bombardment rates, which lie between the minimum and maximum bombardment fits (Pearce et al. 2017; Chyba 1990). These bombardment rates are 1.2×10^{25} g Gyr^{-1} and 1.2×10^{24} g Gyr^{-1} at 4.4 bya and 4.0 bya, respectively. Multiplying the H_2 degassing abundance per unit mass by the mass delivery rates at 4.4 bya and 4.0 bya gives us H_2 impact degassing rates of 2.3×10^{11} cm^{-2} s^{-1} and 2.3×10^{10} cm^{-2} s^{-1} for the early and late Hadean models, respectively.

We model H and H_2 escape using the approximation developed by Zahnle et al. (2019, 2020), which blends energy-limited and diffusion-limited escape. The equation is

$$\left(\frac{dN_{H_2}}{dt} \right)_{esc} = - \frac{AS}{\sqrt{1 + B^2 S^2}} \frac{N_{H_2}}{\Sigma_j N_j} \quad (cm^{-2} s^{-1}) \quad (A2)$$

Table A4

Deposition Velocities for the Chemical Species in Our Early Earth Models

Species	Deposition (cm s^{-1})	Source
CO_2	1×10^{-4}	Archer (2010)
CH_3OH	0.1	Wohlfahrt et al. (2015)
O_2	1×10^{-8}	This work
CO	1×10^{-8}	Kharecha et al. (2005)
H_2O_2	0.5	Hauglustaine et al. (1994)
C_2H_6	1×10^{-5}	Hu et al. (2012)
HO_2	1	Ranjan et al. (2020)
H_2CO	0.1	Wagner et al. (2002)
HCO	0.1	Ranjan et al. (2020)
HCN	7×10^{-3}	Tian et al. (2011)
OH	1	Ranjan et al. (2020)
^3O	1	Ranjan et al. (2020)
H	1	Ranjan et al. (2020)

where $A = 2 \times 10^{12} \text{ cm}^{-2} \text{ s}^{-1}$, $B^2 = 0.006$, S is the extreme-UV and far-UV irradiation relative to the modern Sun (i.e., 30 and 9 for 4.4 and 4.0 bya, respectively), N_{H_2} is the number of H_2 molecules, and N_j is the number of molecules of species j .

The limits of H_2 degassing to assume a static pressure profile in equilibrium with H_2 escape would be $\sim 2.3 \times 10^{13}$ and $1.4 \times 10^{13} \text{ cm}^{-2} \text{ s}^{-1}$ at 4.4 and 4.0 bya, respectively.

We use a constant CO_2 outgassing rate of $3.0 \times 10^{11} \text{ cm}^{-2} \text{ s}^{-1}$ in all our models, which is consistent with Earth-like volcanic outgassing used in other atmospheric models (Hu et al. 2012).

Guzmán-Marmolejo et al. (2013) modeled the production of CH_4 in hydrothermal systems for an Earth-like planet, and calculated a production rate of $6.8 \times 10^8 \text{ cm}^{-2} \text{ s}^{-1}$. Guzmán-Marmolejo et al. (2013) also modeled H_2 production in hydrothermal systems; however, the rates of H_2 produced in hydrothermal environments are orders of magnitude lower than the rates of H_2 production from impact degassing.

We do not include loss of CH_4 due to haze production, as our CH_4/CO_2 ratio never exceeds 0.1 (which is a common identifier for haze production) (Trainer et al. 2006).

In Table A4, we list the deposition velocities for the species that are rained out of the lowest layer in our atmospheric models.

We apply a CO_2 deposition velocity of $1.0 \times 10^{-4} \text{ cm s}^{-1}$, which is estimated in Hu et al. (2012) to produce a CO_2 lifetime consistent with the lifetime of silicate weathering on Earth. We use a CO deposition velocity of $1 \times 10^{-8} \text{ cm s}^{-1}$, calculated from a two-box model (Kharecha et al. 2005). We also use a deposition velocity of $1 \times 10^{-8} \text{ cm s}^{-1}$ for O_2 , given its similar solubility and diffusivity to CO (Harman et al. 2015). We use the standard HCN deposition velocity of $7.0 \times 10^{-3} \text{ cm s}^{-1}$ that is used in other early Earth models (Tian et al. 2011; Zahnle 1986). Additional deposition velocities are chosen to be consistent with other atmospheric models for rocky exoplanets (Hu et al. 2012; Ranjan et al. 2020). Major species not listed in this table (e.g., H_2 and CH_4) are not very soluble in water, therefore we do not include rain-out for these species (Sander 2020).

A.1.1. Lightning

Lightning chemistry in the context of the origin of life was first developed experimentally in the 1950s (Miller 1953). The fundamental Miller–Urey experiment involves sending an

electric discharge through a combination of reduced gases to trigger dissociation. The radicals produced in this process then react to form biomolecule precursors such as HCN and H_2CO (Miller 1957b; Bada 2016). These precursors condense into a reservoir, where aqueous chemistry produces biomolecules such as amino acids (Miller 1953; Bada 2013) and nucleobases (Ferus et al. 2017b).

Present-day Earth has an average global lightning flash density of $\sim 2 \text{ flashes km}^{-2} \text{ yr}^{-1}$ (Hodosán et al. 2016). However, above just the oceans, this average density drops to $0.3\text{--}0.6 \text{ flashes km}^{-2} \text{ yr}^{-1}$. Given the smaller coverage of continental crust above sea water during the Hadean, we set the global lightning flash density for our models to $1 \text{ flash km}^{-2} \text{ yr}^{-1}$; however, we also explore an average lightning flash density measured locally during volcanic eruptions on Earth today ($\sim 10^4 \text{ flashes km}^{-2} \text{ yr}^{-1}$).

We considered both nonequilibrium and equilibrium approaches for modeling lightning chemistry. For our nonequilibrium approach, we integrated the production of key radicals for the first $\sim 40 \mu\text{s}$ of a lightning strike using the pressure and temperature evolution from Ardaseva et al. (2017). However, this approach had accuracy issues as a complete high-temperature reaction network is required to accurately calculate the chemical evolution within a cooling lightning channel. This approach also led to some nonsensical results such as HCN production that is independent of lightning flash density.

Therefore, we use an equilibrium approach for modeling the lightning production of HCN and other species based on the lightning chemistry models for HCN and NO production by Chameides & Walker (1981). Lightning channels heat up to a point ($\sim 30,000 \text{ K}$) (Orville 1968) where the equilibrium timescale is less than $1 \mu\text{s}$ (Hill et al. 1980). In fact, ab initio molecular dynamics simulations of electric discharges suggest the timescale for lightning chemistry may be of the order of picoseconds (Cassone et al. 2018). This is fast compared to the hundred millisecond cooling timescale of a lightning channel, as well as the $10 \mu\text{s}$ eddy diffusion timescale in the lowest layer in our atmospheres.

Chemical abundances rapidly reach equilibrium while the lightning channel is above the freeze-out temperature (T_F). The freeze-out temperature is the temperature at which the concentration of a species can still be described by its equilibrium value. Beyond this point, there is not enough time at a given temperature for equilibrium to be reached, and thus the concentrations are frozen into the gas for the remainder of the cooling of the lightning channel. Reaction rate coefficients that break down a species are used to roughly determine the freeze-out temperature, e.g., $\text{HCN} + \text{MCN} + \text{H} + \text{M}$. Typical freeze-out temperatures range from 1000 to 5000 K. The freeze-out temperature for HCN is $\sim 2000\text{--}2500 \text{ K}$ for lightning strikes similar in energy to Earth today (10^5 J m^{-1}) (Chameides & Walker 1981). Other species such as NO have higher freeze-out temperatures near 3000–3500 K for similar lightning discharge energies, but can also be $\sim 2000 \text{ K}$ for the highest discharge energies (10^{15} J m^{-1}). We adopt $T_F = 2000 \text{ K}$ for our equilibrium calculations to estimate the mixing ratios for HCN and 13 other dominant equilibrium products in the early Earth lightning models by Chameides & Walker (1981).

Equilibrium calculations are performed using the thermochemical data from the JANAF tables (Stull & Prophet 1971),

Table A5

Equilibrium Abundances (Molar Mixing Ratios) from Lightning Chemistry Occurring in Our Four Early Earth Models

Species	Model A	Model B	Model C	Model D
HCN	1.4×10^{-10}	1.8×10^{-13}	5.1×10^{-11}	1.8×10^{-13}
H ₂	8.9×10^{-1}	8.7×10^{-1}	8.9×10^{-1}	8.7×10^{-1}
H	1.3×10^{-3}	6.0×10^{-6}	1.4×10^{-3}	6.0×10^{-6}
N ₂	9.9×10^{-2}	9.8×10^{-2}	9.9×10^{-2}	9.8×10^{-2}
⁴ N	2.3×10^{-10}	2.0×10^{-10}	2.7×10^{-10}	2.0×10^{-10}
H ₂ O	9.9×10^{-3}	9.7×10^{-3}	9.9×10^{-3}	9.7×10^{-3}
³ O	1.4×10^{-9}	3.4×10^{-5}	1.9×10^{-9}	3.4×10^{-5}
OH	1.4×10^{-6}	2.2×10^{-4}	1.6×10^{-6}	2.2×10^{-4}
NO	1.6×10^{-8}	4.6×10^{-4}	1.9×10^{-8}	4.6×10^{-4}
O ₂	6.9×10^{-12}	5.3×10^{-3}	9.1×10^{-12}	5.3×10^{-3}
CH ₄	1.4×10^{-11}	4.2×10^{21}	4.0×10^{-12}	4.2×10^{-21}
CH ₃	5.0×10^{-13}	2.3×10^{-20}	1.6×10^{-13}	2.0×10^{-20}
CO	2.0×10^{-6}	1.1×10^{-2}	9.9×10^{-7}	1.1×10^{-2}
CO ₂	4.8×10^{-9}	8.7×10^{-1}	2.4×10^{-9}	8.7×10^{-1}

Note. Thermodynamic simulations are based on initial concentrations in Table 1 for a freeze-out temperature of $T_F = 2000$ K.

and the ChemApp software library (distributed by GTT Technologies, <http://gtt.mch.rwth-aachen.de/gtt-web/>).

In Table A5, we display the equilibrium mixing ratios based on the initial abundances in our four early Earth models for a freeze-out temperature of $T_F = 2000$ K.

For our fiducial models, we introduce HCN and other species to the bottom layer of the atmosphere at a rate that corresponds to $1 \text{ flash km}^{-2} \text{ yr}^{-1}$. The species influx rates from lightning chemistry are calculated along a lightning channel extending through the first layer of the atmosphere using the following equation:

$$\frac{d[M]}{dA dt} = \frac{n_M P \Delta H \dot{f} \sigma_l}{k_B T \gamma} \left(\frac{1}{100} \right)^3 \left(\frac{1}{10,000} \right)^2, \quad (\text{A3})$$

where $d[M]/dA dt$ is the molar concentration of species M produced per cm^2 per second, n_M is the molar mixing ratio of species M produced in the lightning strike (cm^{-3}), ΔH is the height of the lowest atmospheric layer (cm), \dot{f} is the lightning flash density in flashes $\text{km}^{-2} \text{ yr}^{-1}$, σ_l is the cross section of the lightning channel ($\sim 1 \text{ cm}^2$), $\gamma = 3600 \times 24 \times 365.25 \text{ s yr}^{-1}$, and the remainder is unit conversion.

A.2. Warm Little Pond Models

In Table A6, we display the sources and sinks for nucleobases, ribose, and 2-aminooxazole in our warm little pond models. All biomolecule reaction yields are based on HCN. For cytosine, uracil, thymine, ribose, and 2-aminooxazole, which require formaldehyde as a reactant, we use a formaldehyde yield from HCN of 3.6%, which is three times the glyceronitrile yield from radiolytic aqueous HCN experiments performed by Yi et al. (2020). We assume, to first order, that the UV radiation incident at the pond surface allowed this aqueous photolytic reaction to

proceed with similar yields to the Yi et al. (2020) radiolytic experiments.

We consider two yields for adenine production from HCN in our pond solutions based on experiments: a lower yield of 0.5% based on aqueous reactions of HCN (Oró & Kimball 1961), and an upper yield of 18% based on HCN reactions with more ideal conditions for forming adenine (e.g., solutions containing NH₃ and ammonium formate (Hill & Orgel 2002; Wakamatsu et al. 1966).

For guanine and uracil we consider lower yields of 0.0067% and 0.0017%, respectively, based on experiments of frozen ammonium cyanide solutions (Miyakawa et al. 2002). We use theoretical yields for the upper bounds. Guanine has a theoretical yield of 20% based on the theoretical HCN-based reaction equation $5\text{HCN} + \text{H}_2\text{O} \rightarrow \text{guanine} + \text{H}_2$ (Larowe & Regnier 2008). Uracil has a theoretical yield of 50%; however, this is based on H₂CO as a limiting reagent ($2\text{HCN} + 2\text{H}_2\text{CO} \rightarrow \text{uracil} + \text{H}_2$ (Larowe & Regnier 2008). Experiments of the Kiliani–Fischer synthesis of glyceronitrile produce H₂CO as an intermediate from aqueous solutions of HCN (Yi et al. 2020). Yields of glyceronitrile production are 1.2%; however, theory suggests three intermediate HCN molecules are involved in this reaction. Considering this, we apply a yield of 3.6% for H₂CO production from HCN. For uracil, this results in an upper yield of $50\% \times 3.6\% = 1.8\%$.

Given the lack of experiments producing cytosine and thymine from aqueous HCN, we only consider the theoretical upper yields for these species based on the reaction equations $3\text{HCN} + \text{H}_2\text{CO} \rightarrow \text{cytosine}$ and $2\text{HCN} + 3\text{H}_2\text{CO} \rightarrow \text{thymine} + \text{H}_2\text{O}$ (Larowe & Regnier 2008). Again, since H₂CO is the limiting reagent for these theoretical reactions, we apply the yield of 3.6% for H₂CO production from HCN, resulting in yields of 3.6% and 1.2% for cytosine and thymine production from HCN, respectively.

For 2-aminooxazole, we consider a yield of 0.11% based on radiolytic experiments of aqueous solutions of HCN (Yi et al. 2020).

Finally, experiments of ribose synthesis from H₂CO have identified ribose as a product, but yields remain uncertain. Shapiro (1988) suggests 1% as an upper bound, therefore we consider this yield and also apply the yield of 3.6% for H₂CO production from HCN to obtain an overall yield of 0.036%.

The sink rates for biomolecule photodestruction, seepage, and hydrolysis are chosen to match those modeled in Pearce et al. (2017) so that we can directly compare our results with their calculations of biomolecule concentrations in WLPs from meteorites and interplanetary dust particles. Photodestruction and seepage rates are consistent among all biomolecules given the lack of experimental data for each individual biomolecule in our study. Comparison studies of biomolecule photodegradation show differences of about an order of magnitude in photostability between biomolecules (Poch et al. 2015; Todd et al. 2019). Therefore, we expect approximately an order of magnitude additional uncertainty in our biomolecule concentrations during the dry phase, when irradiation is turned on.

Table A6
Sources and Sinks for the Five Nucleobases, Ribose, and 2-aminooxazole in Our Warm Little Pond Model

Biomolecule	Yield from HCN	Yield Reference	Sinks	Sink Rate	Sink Reference
Adenine	0.005–0.18 ^a	Oró & Kimball (1961), Hill & Orgel (2002), Wakamatsu et al. (1966)	Photodestruction	$1.0 \times 10^{-4} \text{ photon}^{-1}$	Poch et al. (2015)
			Seepage	2.6 mm solution day ⁻¹	Boyd (1982), Pearce et al. (2017)
			Hydrolysis	$5.0 \times 10^{-10} \text{ s}^{-1}$	Levy & Miller (1998)
Guanine	6.7×10^{-5} –0.2 ^b	Miyakawa et al. (2002), Larowe & Regnier (2008)	Photodestruction	$1.0 \times 10^{-4} \text{ photon}^{-1c}$	Poch et al. (2015)
			Seepage	2.6 mm solution day ⁻¹	Boyd (1982), Pearce et al. (2017)
			Hydrolysis	$4.8 \times 10^{-10} \text{ s}^{-1}$	Levy & Miller (1998)
Cytosine	0.036 ^d	Yi et al. (2020), Larowe & Regnier (2008)	Photodestruction	$1.0 \times 10^{-4} \text{ photon}^{-1c}$	Poch et al. (2015)
			Seepage	2.6 mm solution day ⁻¹	Boyd (1982), Pearce et al. (2017)
			Hydrolysis	$1.2 \times 10^{-8} \text{ s}^{-1}$	Levy & Miller (1998)
Uracil	1.7×10^{-5} –0.018 ^{bd}	Miyakawa et al. (2002), Yi et al. (2020), Larowe & Regnier (2008)	Photodestruction	$1.0 \times 10^{-4} \text{ photon}^{-1c}$	Poch et al. (2015)
			Seepage	2.6 mm solution day ⁻¹	Boyd (1982), Pearce et al. (2017)
			Hydrolysis	$1.4 \times 10^{-11} \text{ s}^{-1}$	Levy & Miller (1998)
Thymine	0.012 ^d	Yi et al. (2020), Larowe & Regnier (2008)	Photodestruction	$1.0 \times 10^{-4} \text{ photon}^{-1c}$	Poch et al. (2015)
			Seepage	2.6 mm solution day ⁻¹	Boyd (1982), Pearce et al. (2017)
			Hydrolysis	$2.8 \times 10^{-12} \text{ s}^{-1}$	Levy & Miller (1998)
2-aminooxazole	0.0011	Yi et al. (2020),	Photodestruction	$1.0 \times 10^{-4} \text{ photon}^{-1c}$	Poch et al. (2015)
			Seepage	2.6 mm solution day ⁻¹	Boyd (1982), Pearce et al. (2017)
			Hydrolysis	none ^e	
Ribose	3.6×10^{-4f}	Yi et al. (2020), Shapiro (1988)	Photodestruction	$1.0 \times 10^{-4} \text{ photon}^{-1c}$	Poch et al. (2015)
			Seepage	2.6 mm solution day ⁻¹	Boyd (1982), Pearce et al. (2017)
			Hydrolysis	none ^g	

Notes. HCN enters our ponds from rain-out calculated in our antecedent atmospheric model, and is multiplied by experimental and theoretical yields to simulate the in situ production of key RNA biomolecules. H₂CO, which is a key reactant for cytosine, uracil, and ribose synthesis, is produced in our ponds directly from HCN (Yi et al. 2020). HCN reactions are fast (experiments last less than a few days) in comparison to the duration of our models.

^a Yield range is based on experiments with and without catalysts, e.g., ammonium formate.

^b Lower yield value is from experiment. Upper value is the theoretical yield.

^c Photodestruction rate assumed to be similar to that of adenine.

^d Yield is based on radiolytic experiments for the Kiliani–Fischer synthesis of glyceronitrile (Yi et al. 2020), for which H₂CO is initially produced from irradiated solutions of HCN and water. We multiply the glyceronitrile yield by 3, given 3 times fewer HCN molecules are required for antecedent H₂CO synthesis. H₂CO is then assumed to be the limiting reagent in the theoretical reaction from Larowe & Regnier (2008), for which we assume the 100% theoretical yield.

^e There are no known hydrolysis experiments for 2-aminooxazole; however, it is known to be fairly stable (Szabla et al. 2013). We assume the other two sinks dominate the loss of this species.

^f Ribose yields from lab experiments of the formose reaction are uncertain; however, 1% has been suggested.

^g We assume sufficient borate is present in our ponds to stabilize ribose from hydrolysis (Ricardo et al. 2004).

Appendix B Supplementary Results

B.1. Rain-out Rates

In Figure B1, we display the rain-out rates for HCN, H₂CO, and CO₂ as a function of time. These water-soluble species, and a few others, are removed from the lowest layer of our atmospheric models at each time step. The HCN rain-out rate for the early Hadean (reducing) model A is $1.3 \times 10^{-7} \text{ kg m}^{-2} \text{ yr}^{-1}$ at 50 million years. This is about five orders of magnitude higher than the HCN rain-out rates for the late Hadean

(oxidizing) models of $\sim 10^{-12}$ (same units). The HCN rain-out rate for model C is approximately a factor of 5 lower than that for model A at 10 million years. We use the 50 million year and 800,000 year HCN rain-out rates from models A and B, respectively, for influx into our subsequent warm little pond models.

The H₂CO rain-out rate for the early Hadean (reducing) model A is $6.0 \times 10^{-12} \text{ kg m}^{-2} \text{ yr}^{-1}$ at 50 million years. This is ~ 2 orders of magnitude lower than the H₂CO rain-out rates for the late Hadean (oxidizing) models of $\sim 10^{-9} \text{ kg m}^{-2} \text{ yr}^{-1}$ at 1 million years.

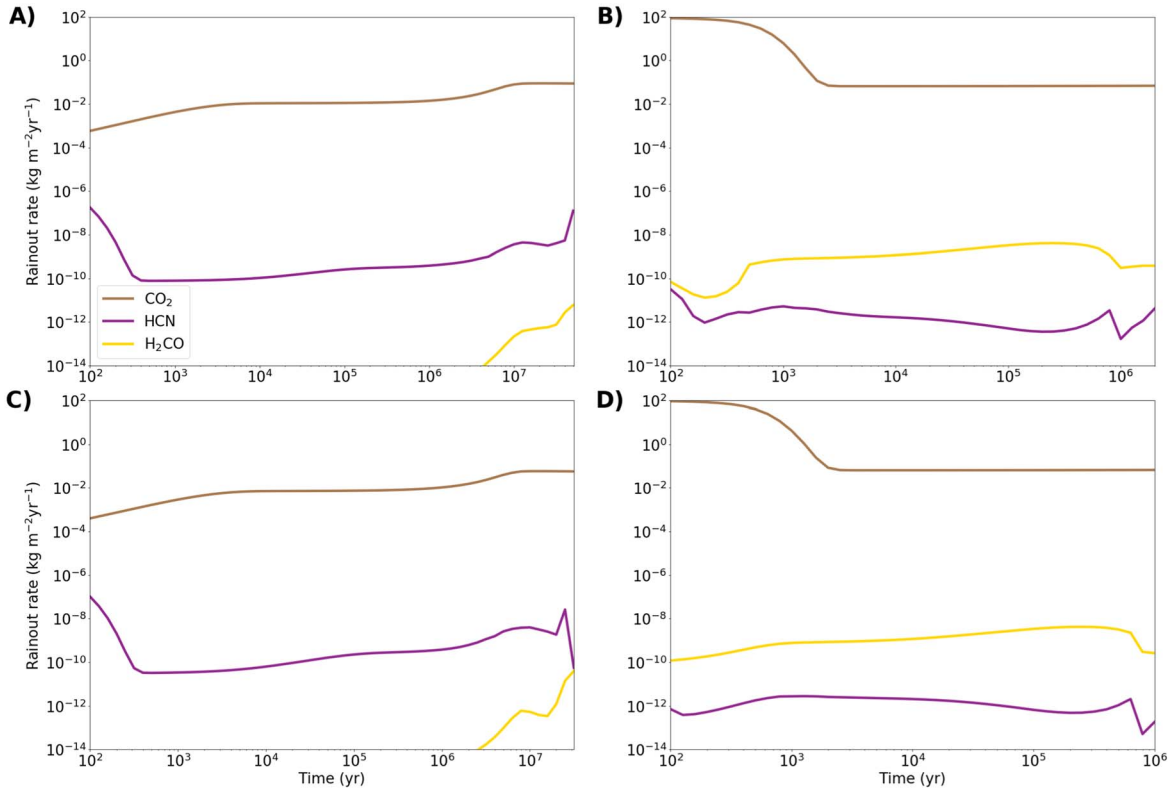


Figure B1. Rain-out rates of HCN, CO₂, and H₂CO from the lowest atmospheric layer as a function of time in our four early Earth models. Model parameters are listed in Table 1.

B.2. HCN to CH₄ Ratio

In Figure B2, we display the molar abundance ratio of HCN/CH₄ in the lowest atmospheric layer from $t = 500$ yr onwards. For the early Hadean (reducing) models A and C, the average HCN/CH₄ ratio during this period is $\sim(1-4) \times 10^{-7}$. For the late Hadean (oxidizing) models B and D, the average HCN/CH₄ ratios are $(3-5) \times 10^{-6}$. The HCN/CH₄ ratios are constant at 10^{-8} for models A and C from $t = 500$ to 1 million years, but vary by up to three orders of magnitude beyond this point. Multiple oxygen species begin to fluctuate in abundance after ~ 1 million years, including H₂O, CO, and OH, which affects HCN production but not the CH₄ abundance. Similarly, fluctuations in species such as O₂ and H₂ in models B and D after $\sim 600,000$ yr cause the HCN/CH₄ ratios to fluctuate beyond this point.

B.3. No Seepage

In Figure B3, we turn off seepage in our model WLPs from Figure 4, and display the results from $t = 0$ to 10,000 yr. This model represents a scenario where the rock pores at the base of the WLP are blocked by, e.g., amphiphilic multilamellar matrices or mineral gels (Deamer 2017; Damer & Deamer 2020). In the absence of seepage, hydrolysis takes over as the main biomolecule sink. We see species with high hydrolysis rates such as cytosine, adenine, and guanine reach a steady state in just a few hundred years. Hydrolysis rates for uracil and thymine are lower, allowing them to build in concentration to near micromolar abundances in 10,000 yr. 2-aminooxazole and ribose are not given hydrolysis rates in our models, and thus their concentrations here are to be considered maxima in the absence of aqueous chemical sinks. We

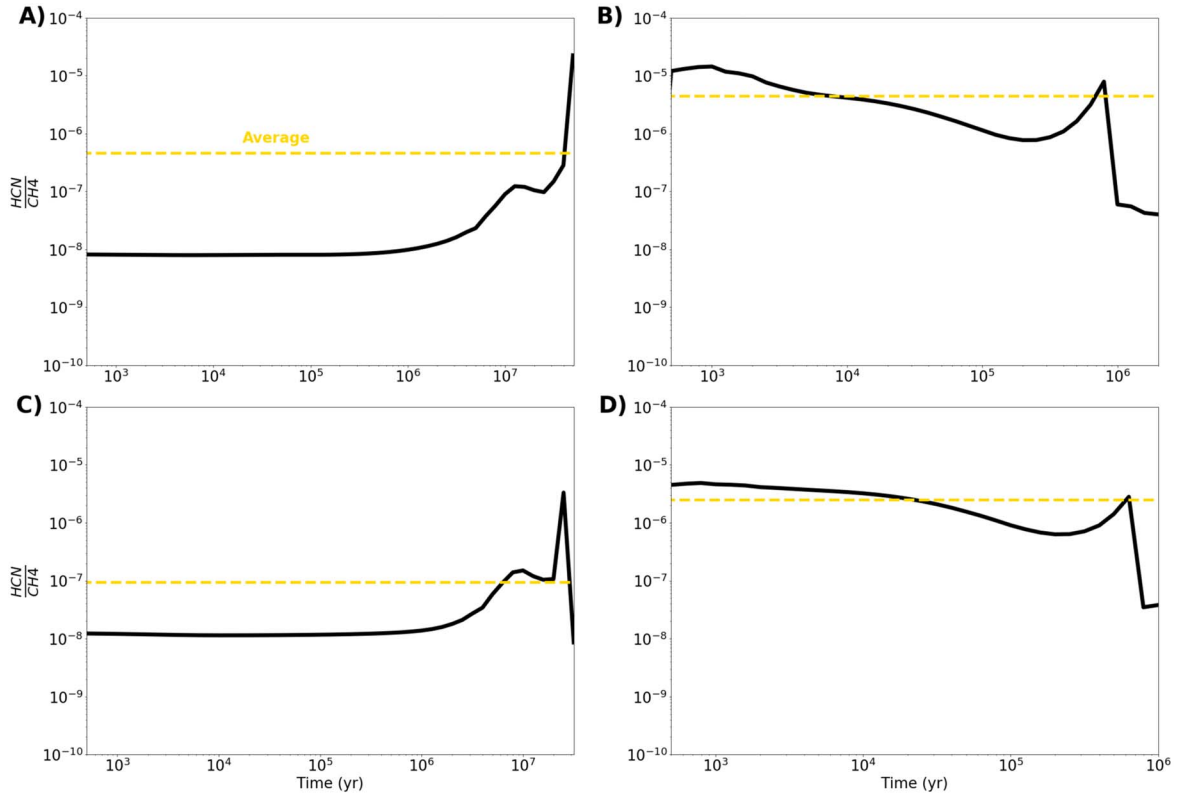


Figure B2. The molar abundance ratio of HCN to CH₄ in the lowest atmospheric layer for our four early Earth models. Model parameters are listed in Table 1.

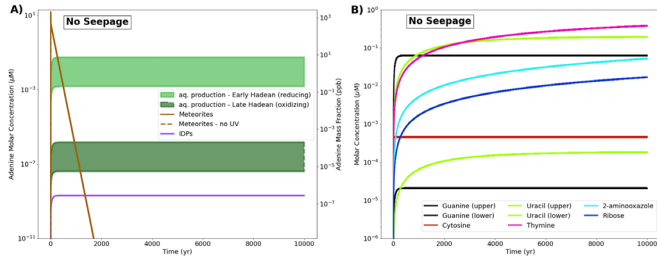


Figure B3. The same as Figure 4, but with seepage turned off.

summarize the no-seepage model biomolecule concentrations at $t = 10,000$ yr in Table B1.

B.4. Biomolecule Concentrations

In Table B1, we display the peak concentrations of biomolecules in our model WLPs for our early Hadean (reducing), late Hadean (oxidizing), and no-seepage models.

B.5. Maximum Lightning Flash Density

In Figure B4, we plot the molar HCN mixing ratio as a function of altitude for our early Hadean (reducing) model A using an increased lightning flash density 10^4 times greater than our fiducial rate. This lightning flash density represents an average value measured near volcanic eruptions on Earth today (Hodosán et al. 2016).

Table B1

Summary of the Peak Concentrations of Biomolecules and Biomolecule Precursors for Our Fiducial Atmosphere and WLP Models

Molecule	Model A (Reducing) (nM)	Model B (Oxidizing) (nM)	Model A (No Seepage) (nM)
HCN	41.5	1.1×10^{-3}	^a
H ₂ CO (aq. production)	1.5	4.1×10^{-5}	^a
H ₂ CO (rain-out)	1.8×10^{-3}	0.34	^a
Adenine	7.3	2.0×10^{-4}	54.9
Guanine	8.2	2.2×10^{-4}	63.3
Cytosine	1.4	3.9×10^{-5}	0.46
Uracil	0.7	2.0×10^{-5}	195
Thymine	0.5	1.3×10^{-5}	383
2-aminooxazole	0.045	$\sim 10^{-6}$	52.6
Ribose	0.015	$\sim 10^{-7}$	17.2

Note. An early Hadean (reducing) model A with seepage turned off is also included (see Figure B1), representing a pond whose base pores are blocked by, e.g., amphiphilic multilamellar matrices or mineral gels (Damer & Deamer 2020; Deamer 2017).

^a We do not estimate hydrolysis rates for this species, which is typically the rate-limiting sink in the absence of seepage.

We see no changes to the HCN profile when using an enhanced lightning flash density. This suggests that volcanically active regions of early Earth would not have higher HCN abundances than the global average from photochemistry.

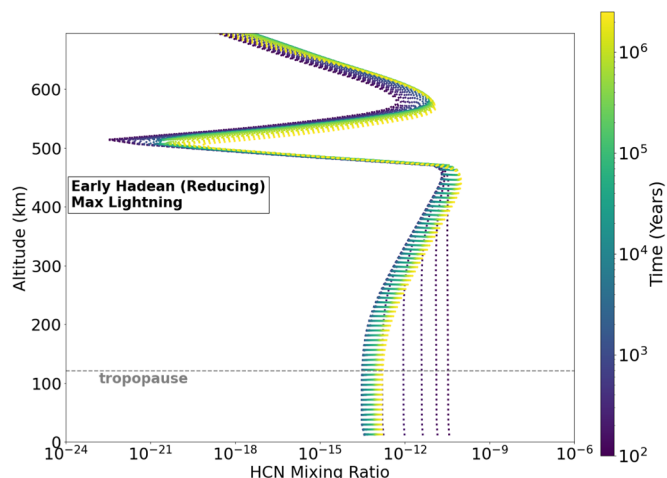


Figure B4. The molar abundance of HCN from $t = 100$ yr to 40 million years for model A with an increased lightning flash density of 10^4 flashes $\text{km}^{-2} \text{yr}^{-1}$. This flash density is a rough average measured during volcanic eruptions on Earth today, and is 10^4 times greater than the global average used in our fiducial models (Hodosán et al. 2016). Model parameters are listed in Table 1.

ORCID iDs

Ben K. D. Pearce <https://orcid.org/0000-0002-5449-4195>

Karan Molaverdikhani <https://orcid.org/0000-0002-0502-0428>

Ralph E. Pudritz <https://orcid.org/0000-0002-7605-2961>

Thomas Henning <https://orcid.org/0000-0002-1493-300X>

References

- Adriani, A., Dinelli, B. M., López-Puertas, M., et al. 2011, *Icar*, **214**, 584
- Archer, D. 2010, *The Long Thaw: How Humans Are Changing the Next 100,000 Years of Earth's Climate* (Princeton, NJ: Princeton Univ. Press)
- Ardaseva, A., Rimmer, P. B., Waldmann, I., et al. 2017, *MNRAS*, **470**, 187
- Arney, G., Domagal-Goldman, S. D., Meadows, V. S., et al. 2016, *AsBio*, **16**, 873
- Atkinson, R., Baulch, D. L., Cox, R. A., et al. 1989, *JPCRD*, **18**, 881
- Bada, J. L. 2013, *Chem. Soc. Rev.*, **42**, 2186
- Bada, J. L. 2016, *Metode Sci. Stud. J.*, **6**, 183
- Baraffe, I., Homeier, D., Allard, F., & Chabrier, G. 2015, *A&A*, **577**, A42
- Baulch, D. L., Cobos, C. J., Cox, R. A., et al. 1992, *JPCRD*, **21**, 411
- Baulch, D. L., Cobos, C. J., Cox, R. A., et al. 1994, *JPCRD*, **23**, 847
- Becker, K. H., Brockmann, K. J., & Wiesen, P. 1988, *J. Chem. Soc. Faraday Trans. 2*, **84**, 455
- Becker, K. H., Kurtenbach, R., Schmidt, F., & Wiesen, P. 2000, *CoFl*, **120**, 570
- Becker, S., Schneider, C., Okamura, H., et al. 2018, *NatCo*, **9**, 163
- Benner, S. A., Bell, E. A., Biondi, E., et al. 2020, *ChemSystemsChem*, **2**, e1900035
- Berghuijs, W. R., & Woods, R. A. 2016, *IJCLi*, **36**, 3161
- Boyd, C. E. 1982, *Trans. Am. Fish. Soc.*, **111**, 638
- Bradley, A. S. 2016, *PNAS*, **113**, 13944
- Bradley, A. S., & Summons, R. E. 2010, *E&PSL*, **297**, 34
- Braun, W., Bass, A. M., Davis, D. D., & Simmons, J. D. 1969, *RSPSA*, **312**, 417
- Breslow, R. 1959, *Tetrahedron Lett.*, **1**, 22
- Buck, A. L. 1981, *JApMe*, **20**, 1527
- Burton, G. R., Chan, W. F., Cooper, G., & Biron, C. E. 1992, *CP*, **167**, 349
- Butlerow, A. 1861, *Ann. Chem. Pharm.*, **120**, 295
- Callahan, M. P., Smith, K. E., Cleaves, H. J., et al. 2011, *PNAS*, **108**, 13995
- Carl, S., Qian, S., Vereecken, L., & Peeters, J. 2000, *JPCA*, **106**, 12242
- Cassone, G., Sponer, J., Sponer, J. E., et al. 2018, *ChCom*, **54**, 3211
- Catling, D., & Kasting, J. F. 2007, in *Planetary Atmospheres and Life*, ed. W. T. Sullivan, III & J. A. Baross (Cambridge: Cambridge Univ. Press), 91
- Catling, D. C. 2015, in *Planetary Atmospheres*, ed. D. C. Catling (2nd ed.; Oxford: Elsevier), 429
- Chameides, W. L., & Walker, J. C. G. 1981, *OrLi*, **11**, 291
- Charnay, B., Wolf, E. T., Marty, B., & Forget, F. 2020, *SSRv*, **216**, 90
- Chyba, C., & Sagan, C. 1992, *Natur*, **355**, 125
- Chyba, C. F. 1990, *Natur*, **343**, 129
- Cicerone, R. J., & Zellner, R. 1983, *JGR*, **88**, 10689
- Cleaves, H. J., Chalmers, J. H., Lazzano, A., Miller, S. L., & Bada, J. L. 2008, *OLEB*, **38**, 105
- Cooper, W. F., & Hersherberger, J. F. 1992, *JPhCh*, **96**, 771
- Cooper, W. F., Park, J., & Hersherberger, J. F. 1993, *JPhCh*, **97**, 3283
- Da Silva, L., Maurel, M.-C., & Deamer, D. 2015, *JMolE*, **80**, 86
- Damer, B., & Deamer, D. W. 2020, *AsBio*, **20**, 429
- Dauphas, N. 2017, *Natur*, **541**, 521
- Deamer, D. W. 2017, *Life*, **7**, 5
- Dorthe, G., Caubet, P., Vias, T., Barrere, B., & Marchais, J. 1991, *JPhCh*, **95**, 5109
- Duncanson, J. A., Jr., & Guillory, W. A. 1983, *JChPh*, **78**, 4958
- Ferus, M., Kubelik, P., Knizek, A., et al. 2017a, *NatSR*, **7**, 6275
- Ferus, M., Pietrucci, F., Saitta, A. M., et al. 2017b, *PNAS*, **114**, 4306
- Ferus, M., Pietrucci, F., Saitta, A. M., et al. 2019, *A&A*, **626**, A52
- Fiebig, J., Woodland, A. B., Spangenberg, J., & Oschmann, W. 2007, *GeCoA*, **71**, 3028
- Frank, P., Bhaskaran, K. A., & Just, T. 1988, *Twenty-First Symp. (Int.) Combust.*, **21**, 885
- Fuller, W. D., Sanchez, R. A., & Orgel, L. E. 1972, *J. Mol. Biol.*, **67**, 25
- Genda, H., Brasser, R., & Mojzsis, S. J. 2017, *E&PSL*, **480**, 25
- Geppert, W. D., Reigier, D., Stoecklin, T., et al. 2000, *PCCP*, **2**, 2873
- Gilbert, W. 1986, *Natur*, **319**, 618
- Glass, G. P., Kumaran, S. S., & Michael, J. V. 2000, *JPCA*, **104**, 8360
- Guillot, T. 2010, *A&A*, **520**, A27
- Guzmán-Marmolejo, A., Segura, A., & Escobar-Briones, E. 2013, *AsBio*, **13**, 550
- Hamouda, S. A., Abdelmalik, M. B., & al-Talhi, E. A.-Q. 2014, *Earth Sci.*, **3**, 26
- Harman, C. E., Schwieterman, E. W., Schottelkotte, J. C., & Kasting, J. F. 2015, *ApJ*, **812**, 137
- Hauglustaine, D. A., Granier, C., Brasseur, G. P., & Mégie, G. 1994, *JGR*, **99**, 1173
- Hébrard, E., Dobrijevic, M., Loison, J. C., Bergeat, A., & Hickson, K. M. 2012, *A&A*, **541**, A21
- Held, I. M., & Soden, B. J. 2000, *Annu. Rev. Energy Environ.*, **25**, 441
- Heller, R., Dude, J.-P., Winkler, M., Reitner, J., & Gizon, L. 2020, *PalZ*, **95**, 563
- Herron, J. T. 1999, *JPCRD*, **28**, 1453
- Hill, A., & Orgel, L. E. 2002, *OLEB*, **32**, 99
- Hill, R. D., Rinker, R. G., & Wilson, H. D. 1980, *JAtS*, **37**, 179
- Hodosán, G., Helling, C., Asensio-Torres, R., Vorgul, I., & Rimmer, P. B. 2016, *MNRAS*, **461**, 3927
- Holm, N. G., Oze, C., Mousis, O., Waite, J. H., & Guilbert-Lepoutre, A. 2015, *AsBio*, **15**, 587
- Hörst, S. M. 2017, *JGRE*, **122**, 432
- Hu, R., Seager, S., & Bains, W. 2012, *ApJ*, **761**, 2
- Husain, D., & Kirsch, L. J. 1971, *Trans. Faraday Soc.*, **67**, 2025
- Husain, D., & Young, A. N. 1975, *J. Chem. Soc. Faraday Trans. 2*, **71**, 525
- Kharcha, P., Kasting, J., & Siefert, J. 2005, *Geobiology*, **3**, 53
- Koskinen, T. T., Yelle, R. V., Snowden, D. S., et al. 2011, *Icar*, **216**, 507
- Krissansen-Totton, J., Olson, S., & Catling, D. C. 2018, *SciA*, **4**, eaao5747
- Lange, E., Lozano, A. I., Jones, N. C., et al. 2020, *JPCA*, **124**, 8496
- Larowe, D. E., & Regnier, P. 2008, *OLEB*, **38**, 383
- Levy, M., & Miller, S. L. 1998, *PNAS*, **93**, 7933
- Lichtin, D. A., Berman, M. R., & Lin, M. C. 1983, *Bull. Soc. Chim. Belg.*, **92**, 656
- Lichtin, D. A., Berman, M. R., & Lin, M. C. 1984, *CPL*, **108**, 18
- Madhusudhan, N. 2012, *ApJ*, **758**, 36
- Magee, B. A., Waite, J. H., Mandt, K. E., et al. 2009, *P&SS*, **57**, 1895
- Manabe, S., & Wetherald, R. T. 1967, *JAtS*, **24**, 241
- Martinotti, F. F., Welch, M. J., & Wolf, A. P. 1968, *ChCom*, **1968**, 115
- McCulloch, M. T., & Bennett, V. C. 1993, *Litho*, **30**, 237
- Messing, I., Sadowski, C. M., & Filseth, S. V. 1979, *CPL*, **66**, 95
- Miller, S. L. 1953, *Sci*, **117**, 528
- Miller, S. L. 1957a, *NYASA*, **69**, 260
- Miller, S. L. 1957b, *Biochim. Biophys. Acta*, **23**, 480
- Miyakawa, S., Cleaves, H. J., & Miller, S. L. 2002, *OLEB*, **32**, 209
- Molaverdikhani, K., Helling, Ch., Lew, B. W. P., et al. 2020a, *A&A*, **635**, A31
- Molaverdikhani, K., Henning, T., & Mollière, P. 2020b, *ApJ*, **899**, 53
- Molaverdikhani, K., Henning, T., & Mollière, P. 2019a, *ApJ*, **883**, 194
- Molaverdikhani, K., Henning, T., & Mollière, P. 2019b, *ApJ*, **873**, 32
- Mollière, P., Stolker, T., Lacour, S., et al. 2020, *A&A*, **640**, A131
- Mollière, P., van Boekel, R., Dullemond, C., Henning, T., & Mordasini, C. 2015, *ApJ*, **813**, 47
- Mollière, P., Wardenier, J. P., van Boekel, R., et al. 2019, *A&A*, **627**, A67

- Morasch, M., Mast, C. B., Langer, J. K., Schilcher, P., & Braun, D. 2014, *ChemBioChem*, 15, 879
- Nam, I., Nam, H. G., & Zare, R. N. 2018, *PNAS*, 115, 36
- Oró, J. 1961, *Natur*, 191, 1193
- Oró, J., & Kimball, A. P. 1961, *Arch. Biochem. Biophys.*, 94, 217
- Orville, R. E. 1968, *JATIS*, 25, 839
- Parmentier, V., & Guillot, T. 2014, *A&A*, 562, A133
- Pearce, B. K. D., Ayers, P. W., & Pudritz, R. E. 2019, *JPCA*, 123, 1861
- Pearce, B. K. D., Ayers, P. W., & Pudritz, R. E. 2020a, *JPCA*, 124, 8594
- Pearce, B. K. D., Molaverdikhani, K., Pudritz, R. E., Henning, T., & Hébrard, E. 2020b, *ApJ*, 901, 110
- Pearce, B. K. D., & Pudritz, R. E. 2015, *ApJ*, 807, 85
- Pearce, B. K. D., & Pudritz, R. E. 2016, *AsBio*, 16, 853
- Pearce, B. K. D., Pudritz, R. E., Semenov, D. A., & Henning, T. 2017, *PNAS*, 114, 11327
- Pearce, B. K. D., Tupper, A. S., Pudritz, R. E., & Higgs, P. G. 2018, *AsBio*, 18, 343
- Piani, L., Marrocchi, Y., Rigaudier, T., et al. 2020, *Sci*, 369, 1110
- Pinto, J. P., Gladstone, G. R., & Yung, Y. L. 1980, *Sci*, 210, 183
- Poch, O., Jaber, M., Stalport, F., et al. 2015, *AsBio*, 15, 221
- Ponnamperuma, C., Sagan, C., & Mariner, R. 1963, *Natur*, 199, 222
- Powner, M. W., Gerland, B., & Sutherland, J. D. 2009, *Natur*, 459, 239
- Ranjan, S., Schwieterman, E. W., Harman, C., et al. 2020, *ApJ*, 896, 148
- Reichle, R. H., Koster, R. D., De Lannoy, G. J. M., et al. 2011, *JCLI*, 24, 6322
- Ribas, I., Guinan, E. F., Güdel, M., & Audard, M. 2005, *ApJ*, 622, 680
- Ricardo, A., Carrigan, M. A., Olcott, A. N., & Benner, S. A. 2004, *Sci*, 9, 196
- Rich, A. 1962, in *On the Problems of Evolution and Biochemical Information Transfer*, ed. M. Kasha & B. Pullman (New York: Academic), 103
- Rimmer, P. B., & Rugheimer, S. 2019, *Icar*, 329, 124
- Ritson, D. J., Battilocchio, C., Ley, S. V., & Sutherland, J. D. 2018, *NatCo*, 9, 1821
- Robinson, T. D., & Catling, D. C. 2014, *NatGe*, 7, 12
- Roesch, A., Wild, M., Pinker, R., & Ohmura, A. 2002, *JGRD*, 107, 4221
- Rosing, M. T., Bird, D. K., Sleep, N. H., & Bjerrum, C. J. 2010, *Natur*, 464, 744
- Ross, D. S., & Deamer, D. 2016, *Life*, 6, 28
- Saladino, R., Bizzarri, B. M., Botta, L., et al. 2017, *NatSR*, 7, 14709
- Sander, R. 2020, in *Henry's Law Constants*, ed. P. J. Linstrom & W. G. Mallard (Gaithersburg, MD: National Institute of Standards and Technology)
- Schacke, H., Schmatjko, K., & Wolfrum, J. 1974, *Arch. Proces. Spalania*, 5, 363
- Schlesinger, A., & Miller, S. L. 1983, *JMoIE*, 19, 376
- Shapiro, R. 1988, *OrLi*, 18, 71
- Sleep, N. H. 2010, *Cold Spring Harbor Perspect. Biol.*, 2, a002527
- Stempleman, R. S. 1983, in *IMACS Transactions of Scientific Computation*, Vol. 1, ODEPACK, A Systematized Collection of ODE Solvers, ed. R. S. Stepleman (Amsterdam: North-Holland), 55
- Stull, D. R., & Prophet, H. 1971, *JANAF Thermochemical Tables*, NSRDS-NBS 37 (Washington, DC: U.S. Gov. Print. Off.)
- Szabla, R., Šponer, J. E., Šponer, J., & Góra, R. W. 2013, *PCCP*, 15, 7812
- Teichert, J. S., Kruse, F. M., & Trapp, O. 2019, *AngCh*, 131, 10049
- Thuillier, G., Floyd, L., Woods, T. N., et al. 2004, *AdSpR*, 34, 256
- Tian, F., Kasting, J. F., & Zahnle, K. 2011, *E&PSL*, 308, 417
- Todd, Z. R., Szabla, R., Szostak, J. W., & Sasselov, D. D. 2019, *ChCom*, 55, 10388
- Trail, D., Watson, E. B., & Tailby, N. D. 2011, *Natur*, 480, 79
- Trainer, M. G., Pavlov, A. A., DeWitt, H. L., et al. 2006, *PNAS*, 103, 18035
- Tsang, W., & Hampson, R. F. 1986, *JPCRD*, 15, 1087
- Vinatier, S., Bézard, B., Nixon, C. A., et al. 2010, *Icar*, 205, 559
- Wagner, V., von Glasow, R., Fischer, H., & Crutzen, P. J. 2002, *JGRD*, 107, 4029
- Wakamatsu, H., Yamada, Y., Saito, T., Kumashiro, I., & Takenishi, T. 1966, *J. Org. Chem.*, 31, 2035
- Wang, J., Wang, J. J., Ma, B., et al. 2020, *AJ*, 160, 150
- Wohlfahrt, G., Amelynck, C., Ammann, C., et al. 2015, *ACP*, 15, 7413
- Yi, R., Tran, Q. P., Ali, S., et al. 2020, *PNAS*, 117, 13267
- Zahnle, K. J. 1986, *JGR*, 91, 2819
- Zahnle, K. J., Gacesa, M., & Catling, D. C. 2019, *GeCoA*, 244, 56
- Zahnle, K. J., Lupu, R., Catling, D. C., & Wogan, N. 2020, *PSJ*, 1, 11